

THE TRANSITION FROM OXYGEN-RICH TO CARBON STARS¹

S. JOSEPHINE CHAN AND SUN KWOK

Department of Physics, University of Calgary, Calgary, Alberta, Canada

Received 1988 January 12; accepted 1988 April 27

ABSTRACT

Carbon stars can be identified by optical, infrared, and radio means, but the interrelationships among the groups so selected have not been clear. Recently, Willems and de Jong have suggested that optical carbon stars represent an intermediate evolutionary phase after the termination of mass loss during the oxygen-rich phase and before the carbon-enriched mass loss during the infrared carbon star phase. We have calculated evolutionary tracks for the transition from oxygen-rich to carbon-rich stars based on the model of Willems and de Jong. We find that model spectra produce excellent fits to the observed energy distributions of carbon stars. By comparing observed data with the models, the mass-loss rate and the time since shell detachment can be determined for each individual object.

Subject headings: stars: carbon — stars: evolution

I. INTRODUCTION

Current theories of stellar evolution predict that stars with initial mass less than $8 M_{\odot}$ pass through two phases of red giant evolution (Iben and Renzini 1983). The second red giant phase is referred to as the asymptotic giant branch (AGB) phase. This name originated from the fact that the temperature-luminosity (T_{\star} - L) relationship for low-mass ($< 1 M_{\odot}$) stars asymptotically approaches the T_{\star} - L relationship for stars on the first giant branch (Iben and Renzini 1983). AGB stars develop a degenerate carbon-oxygen inert core which is not large enough to initiate carbon nuclear reactions. At the base of the very extended envelope of the AGB star, hydrogen and helium burn alternately in shells. The hydrogen nuclear reaction produces a helium-rich region which ignites at intervals to produce a double shell burning structure. These helium shell flashes (or thermal pulses) are of short duration. The products of both α -capture and slow-neutron capture (s -process) are carried to the surface. After a sufficient number of "dredge-up" episodes have occurred, the amount of carbon may exceed the amount of oxygen, thus producing a carbon star.

The thermal-pulse scenario proposed by Iben (1975, 1985, 1987) and by Iben and Renzini (1983, 1984) is applicable only to stars of large core mass ($M_c > 0.75 M_{\odot}$), i.e., to AGB stars with $M_{\text{bol}} \sim -6.0$. If the core is not large enough, carbon cannot be dredged up to the surface. But if the above core-mass limitation is satisfied and if the dredge-up process can continue long enough, then, after a few dredge-up episodes, the abundance of ^{12}C will exceed the abundance of ^{16}O and the star will become a carbon star. A carbon star is defined as a star with a photospheric abundance of carbon greater than that of oxygen ($[\text{C}]/[\text{O}] > 1$).

However, observational studies of carbon stars in the Magellanic Clouds (Blanco, Blanco, and McCarthy 1978; Cohen *et al.* 1981; Blanco, McCarthy, and Blanco 1980) suggest that the observed $\langle M_{\text{bol}} \rangle$ of carbon stars is -4.8 , much smaller than the predicted $\langle M_{\text{bol}} \rangle$ of -6.0 . Accordingly, Iben and Renzini (1982*a, b*) have suggested that this discrepancy can be resolved by taking into account the opacity due to the

photoionization of partly recombined carbon in the carbon-enriched region in small-core-mass and low-luminosity ($M_{\text{bol}} \sim -4$) AGB stars. Models including semiconvection and convective overshooting, by Lattanzio (1986), are also able to produce carbon stars at lower luminosities.

Carbon stars are recognized primarily on the basis of the Swan bands of C_2 in their visible photospheric spectra, while cool oxygen-rich stars show bands of metallic oxides. A comprehensive discussion on the spectral classification of carbon stars can be found in Yamashita (1972, 1975).

The *Two Micron Sky Survey* (Neugebauer and Leighton 1969) and the *Air Force Geophysical Laboratory Infrared Sky Survey* (Price and Walker 1976) have detected many late-type stars with strong infrared excesses. Ground-based follow-up observations of these infrared sources found that many of the oxygen-rich stars show the $9.7 \mu\text{m}$ circumstellar silicate feature (Merrill and Stein 1976). However, a number of infrared sources have no silicate feature, the most famous example being CW Leo (IRC + 10216). Radio surveys have found that many of these featureless infrared sources show strong emission in the rotational lines of CO (cf. Zuckerman 1980; Knapp 1987). Many of these CO-emitting stars also have other carbon-based molecules in the circumstellar envelope (Olofsson 1987), some of which have very high molecular weight (e.g., HC_{11}N ; Bell *et al.* 1982). This has led to the interpretation that these infrared sources are carbon stars with most of the oxygen atoms in the form of CO rather than silicate grains. The carbon-rich nature of CW Leo was confirmed by the detection of photospheric CN bands but not oxides (Lockwood 1970; Miller 1970).

The presence of two separate sets of carbon stars—one selected by optical spectra, the other by infrared and radio—has never been carefully investigated, let alone reconciled. Their different properties have, however, recently been brought into focus by the *IRAS* infrared sky survey. Thronson *et al.* (1987) find that the optically classified carbon stars have similar $25 \mu\text{m}/12 \mu\text{m}$ color excesses but varying $60 \mu\text{m}/25 \mu\text{m}$ excesses. Zuckerman and Dyck (1986*b*), however, find that the radio carbon stars are mostly distributed along the blackbody line. A controversy has emerged as to which set represents the "real" population of carbon stars (Zuckerman 1987).

The resolution of the nature of carbon stars has to rely on a

¹ Publication of the Rothney Astrophysical Observatory, No. 52.

full analysis of the optical, infrared, and radio properties of these objects. This was initiated in the thesis of Willems (1987), who analyzed the infrared properties of cataloged carbon stars using data from the *Infrared Astronomical Satellite (IRAS)* low-resolution spectrometer. Most interestingly, he finds that there are a number of photospherically classified carbon stars which show the $9.7 \mu\text{m}$ silicate feature in the circumstellar spectrum. This is interpreted by Willems as evidence of an evolutionary connection between oxygen- and carbon-rich stars. Specifically, he suggests that the carbon stars develop after an oxygen-rich, mass-losing episode on the AGB, and that the carbon star phase represents a change from the formation of oxygen-based grains (silicates) to carbon-based grains in the circumstellar envelope. In this paper, we follow and expand on the original idea of Willems to calculate the evolutionary tracks and circumstellar spectra of carbon stars. Using the photometric and spectroscopic observations of *IRAS* as our data base, we show that Willems's theory can explain many of the observed characteristics of carbon stars and that the differing properties of visible and radio carbon stars can be reconciled.

II. CATALOGS OF CARBON STARS

a) Optical Identification of Carbon Stars

The majority of known carbon stars have been discovered by objective-prism surveys in the optical and near-infrared regions (Stephenson 1965, 1973, 1985; MacConnell 1979, 1982; Hardorp, Lübeck, and Stephenson 1973; Westerlund 1971; Kurtanidze and West 1980; Fuenmayor 1981). A major carbon star catalog (*A General Catalogue of Cool Carbon Stars*, hereafter GCCCS), containing 3219 carbon stars, was published by Stephenson in 1973. In this paper, we will refer to the carbon stars which were found in the optical and near-infrared regions as visual carbon stars.

b) Infrared Identification of Carbon Stars

The $11.2 \mu\text{m}$ silicon carbide (SiC) dust feature was discovered by Treffers and Cohen (1974), and its presence in the circumstellar shells of carbon stars was supported by Forrest, Gillett, and Stein (1975). In the recent *IRAS* all-sky survey, the low-resolution spectrometer (LRS) on *IRAS* identification 538 sources as carbon stars on the basis of the presence of the $11.2 \mu\text{m}$ feature (*IRAS Science Team* 1986). The *IRAS* spectral classification assigns a two-digit number to each LRS spectrum. All SiC sources are designated with a first digit of 4 and a second digit of 1–9 in proportion to the strength of the feature. The classification of other LRS sources is described in the *IRAS Explanatory Supplement* (1985). In this paper, these infrared carbon stars will be referred to as class 40 objects.

c) Radio Identification of Carbon Stars

CO is the most stable molecule in the stellar and interstellar environment. In a stellar atmosphere where the photospheric temperature is low enough for CO to form, most of the carbon is locked into in CO in an oxygen-rich star and most of the oxygen in the form of CO in a carbon star. The CO molecules are ejected as part of the gaseous component of the stellar wind, and the thermal emission lines of CO can be detected by radio techniques.

Circumstellar CO rotational lines ($J = 1-0$ and $J = 2-1$) have been detected in more than 100 evolved stars (cf. Knapp 1987). While CO emissions are present in the circumstellar

envelopes of oxygen-rich stars, they are particularly strong in carbon stars. It is estimated that about 50% of the stars detected with CO in the radio are carbon-rich. However, Hacking *et al.* (1985) find $\sim 85\%$ of his sample of 260 high Galactic latitude stars to be oxygen-rich, in comparison with $\sim 13\%$ carbon-rich. In the study of Thronson *et al.* (1987), the authors estimate that the ratio of dusty oxygen stars to dusty carbon stars is ~ 9 .

The radio technique is particularly useful because some AGB stars have such high mass-loss rates that their photospheres are completely obscured by circumstellar dust. The CO detection rate among carbon stars is higher probably because the CO abundance is 2–3 times higher in carbon stars than in oxygen-rich stars (Knapp and Morris 1985; Zuckerman, Dyck, and Claussen 1986). The radio detection of CO thus serves as a possible means of identifying carbon stars when no photospheric classification is possible.

As of 1987, 169 stars have been detected with circumstellar CO, and these detections are summarized in Table 1. Also listed in Table 1 are the *IRAS, Air Force Geophysical Laboratory Infrared Sky Survey* (AFGL; Price and Walker 1976), *Two Micron Sky Survey* (IRC; Neugebauer and Leighton 1969), GCCCS, and *General Catalogue of Variable Stars* (GCVS; Kukarkin *et al.* 1969) catalog numbers; the LRS classification; and photospheric spectral types where available. Approximately 50% of CO-emitting stars are oxygen-rich. Among the remaining objects, there is not a complete overlap among the radio, infrared, and visual carbon star samples. For example, most of the *IRAS* sources detected as having CO (Leahy, Kwok, and Arquilla 1987; Nguyen *et al.* 1987) are not in the GCCCS. Conversely, many of the visual carbon stars are not known CO sources.

III. COLOR DISTRIBUTIONS OF VISUAL, INFRARED, AND RADIO CARBON STARS

One of the ways to determine the relationship among the visual, infrared, and radio carbon stars is to compare their distributions in a color-color diagram. Of the 1343 carbon stars in the GCCCS which are listed in the *IRAS Point Source Catalog*, 369 have good-quality fluxes at 12, 25, and $60 \mu\text{m}$, and 91 have good fluxes in all four *IRAS* bands including $100 \mu\text{m}$. Among the 369 sources with three good bands, 22 have LRS classification number 01–09 (hereafter referred to as class 00, and similarly for the other classes), 55 are in class 10, 16 in class 20, 2 in class 30, 128 in class 40, 2 in class 50, and 144 have no LRS classification. Figures 1a and 1b show the color distribution of these visual carbon stars. Almost all of them are located above the blackbody line. This fact was noted by Thronson *et al.* (1987) as well as by van der Veen and Habing (1988).

There are 538 class 40 objects in the *Low-Resolution Spectrometer Catalog* (LRSC). However, some of them are confused with H II regions, and others are oxygen-rich stars with $10 \mu\text{m}$ silicate absorption features misidentified by *IRAS* as $11.2 \mu\text{m}$ SiC features in emission (H. Walker 1988, private communication). After the rejection of 26 such sources, the remaining 512 sources are made up of 433 with good photometric fluxes in the *IRAS* 12, 25, and $60 \mu\text{m}$ bands, and 111 objects with good photometric fluxes in all four of the *IRAS* bands. Figure 2a shows the color distribution of the 111 class 40 objects which have good fluxes at all bands. These sources are located at the lower left corner of the diagram.

The color distribution of our sample of 111 class 40 sources has the shape of a "C" on the $12/25/60 \mu\text{m}$ color-color

TABLE 1
LATE-TYPE STARS DETECTED AS HAVING CO EMISSION

IRAS	RAFGL	IRC	C	GCVS	LRS	Var	Sp	Ref	IRAS	RAFGL	IRC	C	GCVS	LRS	Var	Sp	Ref
00042+4248	14	+40004	-	-	26	0	-	6	06291+4319	954	-	-	-	43	55	C	1
00205+5530	57	+60009	-	T Cas	15	50	M7e	1	06300+6058	956	+60169	-	-	28	99	M9	6
00210+6221	-	-	-	-	12	15	-	4	06331+3829	966	40158	537	UU Aur	43	6	N0	1,6,8
00213+3817	59	+40009	-	R And	-	0	S4	6	06342+0328	971	-	-	-	43	99	C	1
01037+1219	157	+10011	-	-	-	18	-	6	06391-2213	4521S	-20101	-	-	23	8	-	3
01085+3022	168	+30021	-	-	29	52	M	1	06500+0829	1028	+10143	-	GX Mon	28	99	M9	1
01133+2530	188	+30025	63	Z Psc	22	0	N0	8	07098-2012	1085	-	-	-	43	95	C	1
01144+6658	190	-	-	-	21	31	C	1	07134+1005	-	-	-	-	-	0	G5	1
01159+7220	194	+70024	-	S Cas	22	11	S4	1	07209-2540	1111	-30087	-	VY CMa	24	6	M5e	1
01246-3248	215	-30015	68	R Scl	-	14	Nb	1,6	07217-1246	-	-	-	-	42	99	-	5
01556+4511	278	+50049	-	-	22	69	Mb	1	07245+4605	1120	+50180	-	Y Lyn	23	25	Mb	7
02143+4404	310	+40037	-	W And	22	12	S6.1e	1	07399-1435	5237	-	-	-	79	99	-	6
02152+2822	-	-	-	-	43	80	C	1	07582-1933	-	-	-	-	44	86	-	5
02168-0312	318	00030	-	o Cet	-	3	M5e	1,6	08045-1524	-	-	-	-	44	95	-	5
02270-2619	337	-30021	103	R For	43	45	Ce	1	08074-3615	-	-	-	-	22	99	C	1
02293+5748	341	-	-	-	42	24	C	1	08088-3243	1235	-	1081	-	-	85	C	1
02316+6455	349	+60092	-	-	-	14	M9	1	08171-2134	5250	-	-	-	22	99	C	1
02351-2711	357	-30023	-	-	29	50	M9	1	08525+1725	1298	+20206	1338	X Cnc	42	59	Nb	8
03186+7016	482	-	-	-	42	99	-	6	09076+3110	1326	+30209	-	RS Cnc	22	7	M6	6
03229+4721	489	+50096	142	-	44	99	-	6	09116-2439	5254	-	-	-	42	97	C	1
03374+6229	505	+60124	154	U Cam	45	5	Nb	1,8	09371+1212	-	-	-	-	-	-	M4(S)	3
03448+4432	5102	-	-	-	42	99	C	1	09425+3444	1376	+30215	-	R LMi	24	99	M7e	6
03507+1115	529	+10050	-	IK Tau	26	6	M6e	6	09429-2148	5259	-20197	-	IW Hya	28	5	M9	1
04020-1551	542	-20049	-	V Eri	22	1	M6	1	09448+1139	1380	+10215	-	R Leo	-	92	M7e	6
04307+6210	595	+60144	-	-	45	99	C	1,6	09452+1330	1381	+10216	-	-	43	99	C(M)	1,6,7
04395+3601	-	-	-	-	62	23	-	6	10131+3049	1403	+30219	1641	-	04	29	C(SR)	1,6
04459+6804	633	+70055	240	ST Cam	42	5	Nb	8	10350-1307	1427	-10242	1714	U Hya	-	0	N2	1
04530+4427	-	-	-	-	42	12	C	1,5	10416+6740	1433	+70100	1736	VY UMa	42	23	N0	8
04566+5606	664	+60150	-	TX Cam	27	99	M8*	6,7	10491-2059	1439	-20218	1766	V Hya	-	0	N	1,6
04573-1452	667	-10080	276	R Lep	45	97	N8	1	10580-1803	1450	-20222	-	R Crt	22	2	M2	1
05028+0106	683	00066	284	W Ori	44	11	Nb	1,8	11308-1020	-	-	-	-	44	0	-	5
05073+5248	700	+50137	-	-	24	99	-	6	11461-3542	4136	-	-	-	22	0	Mb	1
05104+2055	-	-	-	-	42	99	-	5	12427+4542	1576	+50219	2030	Y CVn	42	61	N3	1,6,7,8
05132+5331	715	+50141	-	R Aur	15	99	M7e	6	12447+0425	1579	+00224	2032	RU Vir	44	0	C	6
05136+4712	-	-	-	-	43	56	-	5	12544+6615	1588	+70166	2047	RY Dra	41	43	Np	8
05151+6312	724	+60154	-	-	29	99	M9	1	13001+0527	1594	+10262	-	RT Vir	21	27	Map	1
05238+3406	748	+30114	336	S Aur	45	79	N3e	1	13114-0232	1606	00230	-	SW Vir	-	0	Mb	1,7
05405+3240	809	-	-	-	42	99	C	1,6	13269-2301	1627	-20254	-	R Hya	15	12	M7e	1,7
05411+6957	811	+70066	-	-	29	99	M8	6	13462-2807	1650	-30207	-	W Hya	02	5	M8e	1,7
05426+2040	5168	+20121	393	Y ₁ Tau	45	5	N3	1,8	14219+2555	1706	+30257	-	RX Boo	-	29	M8	6
05524+0723	836	+10100	-	o ₁ Ori	02	24	M0	6	15477+3943	5311	+40273	2293	V CrB	-	67	N3e	1
05559+3825	850	+40149	-	-	27	99	M9	6	16011+4722	5317	+50248	-	X Her	24	7	Mc	1,7
06012+0726	865	-	-	-	22	81	C	6	16105-4205	-	-	-	-	35	99	M	1
06077+2601	-	+30143	461	TU Gem	-	7	N0	8	16269+4159	1864	+40283	-	g Her	16	50	Mb	1,7
06230-0930	935	-	-	-	44	0	C	1	17049-2440	1922	-	-	-	42	92	C	1,6

TABLE 1—Continued

IRAS	RAFGL	IRC	C	GCVS	LRS	Var	Sp	Ref	IRAS	RAFGL	IRC	C	GCVS	LRS	Var	Sp	Ref
17103-3702	-	-	-	-	96	48	-	1	19474-0744	2461	-10524	-	GY Aql	28	99	gM6e	7
17150-3224	6815S	-	-	-	74	6	M	1	19475+3119	-	-	-	-	-	7	-	3
17217-3916	-	-	-	-	42	99	-	5	19477+2401	-	-	-	-	-	6	-	4
17297+1747	1977	20326	-	-	14	99	M2	6	19486+3247	2465	+30395	-	χ Cyg	-	99	M7e	1,6
17334+1537	1988	+20328	-	MW Her	29	99	M(M)	1	19500-1709	-	-	-	-	05	3	F8	3
17371-3021	-	-	-	-	42	99	-	5	19550-0201	2479	00458	-	RR Aql	27	99	M7e	1
17411-3154	5379	-	-	-	-	91	M?	1	19594+4047	2494	-	-	-	42	98	C	1,6
17436+5003	5384	-	-	-	05	35	F8p	3	20028+3910	-	-	-	-	50	5	M?	1
17534-3030	5416	-	-	-	21	97	C?	1	20077-0625	2514	-10529	-	-	23	60	-	6
17534+2603	2028	-	-	V441 Her	23	0	F5p	3	20396+4757	2632	+50338	2923	V Cyg	44	19	Nb	1,6
17556+5813	2040	+60255	2512	T Dra	45	99	C8e	6	20532+5554	-	-	-	-	42	99	-	2
17581-1744	-	-	-	-	44	99	-	2,5	20570+2714	2686	-	-	-	42	98	C	1
18194-2708	2135	-	-	-	43	99	C	6	21032-0024	2702	+00499	2968	RV Aqr	45	97	Ne	6
18239-0655	2154	-	-	-	43	92	C	1	21147+5110	-	-	-	-	42	88	-	2
18240+2326	2155	-	-	-	42	99	-	6	21223+5114	-	-	-	-	42	82	-	2
18248-0839	-	-	-	-	43	99	-	5	21318+5631	-	-	-	-	21	41	M?	1
18269-1257	-	-	-	-	43	99	-	5	21320+3850	2781	+40485	3041	-	44	0	-	6
18333+0533	2199	-	-	-	42	99	-	6	21358+7823	2785	+80048	3055	S Cep	-	0	N8e	1
18349+1023	2206	+10365	-	V1111 Oph	26	97	-	6	21399+3516	2793	+40489	3060	V460 Cyg	42	0	Nb	8
18397+1738	2232	+20370	-	-	43	99	C	1,6,7	21412+3747	2798	+40491	3063	RV Cyg	-	-	N5	8
18398-0220	2233	+00365	2642	-	42	99	C	1	21439-0226	2806	00509	-	EP Aqr	23	15	Mb	1
18413+1354	2241	+10374	-	-	29	99	M7	1	21440+7324	2805	+70177	3070	PQ Cep	44	81	-	1
18424+0346	-	-	-	-	44	97	-	2	21449+4950	-	-	-	-	42	68	N	2
18475+0926	2259	-	-	-	42	99	C	1	21489+5301	-	-	-	-	42	99	C	1
18560-2954	2289	-30398	-	-	27	99	M	1	21554+6204	-	-	-	-	38	14	M	1
18595-3947	5552	-	-	RS CrA	26	99	M	1	22017+2806	2837	+30481	-	TW Peg	26	5	M8	1
19008+0726	2301	+10401	2694	-	43	3	C	1	22035+3506	2845	+40501	-	SV Peg	21	22	Mc	1
19017-0545	2314	-10486	2695	V Aql	42	0	Np	8	22097+5647	2865	+60345	-	CU Cep	29	15	M5	1
19039+0809	2324	+10406	-	R Aql	23	99	M6e	7	22241+6005	2901	-	-	-	41	52	C	1
19059-2219	2330	-20540	-	V3880 Sgr	28	99	M	1	22272+5435	-	-	-	-	72	3	K5	1
19068+0544	-	-	-	-	45	99	-	5	22556+5833	2999	-	-	-	29	16	M	1
19114+0002	2343	-	-	-	-	4	G5	1,3	22585+6402	3011	-	-	-	43	33	C	1
19126-0708	2349	-10497	-	W Aql	22	99	S4	6	23166+1655	3068	-	-	-	02	4	C	1,6
19161+2343	2362	-	-	-	31	99	M	1	23257+1038	3099	-	-	-	-	1	-	6
19175-0807	2368	-10502	-	-	43	99	C	1,6	23268+6854	-	-	-	-	13	4	-	4
19233+7627	2384	+80036	2738	UX Dra	23	0	Nb	8	23320+4316	3116	+40540	-	-	42	0	C	1,6
19321+2757	2417	+30374	-	V1129 Cyg	43	97	C	1	23321+6545	-	-	-	-	05	0	-	3
19346+1209	-	-	-	-	43	99	-	2	23438+0312	3147	00532	3202	TX Psc	-	0	N0	1,8
19354+5005	2422	+50301	-	R Cyg	22	86	S4	1,6	23558+5106	3188	+50484	-	R Cas	24	12	M7e	6
19454+2920	-	-	-	-	05	23	-	3,4									

REFERENCES.—(1) Zuckerman and Dyck 1986a, b; Zuckerman, Dyck, and Claussen 1986. (2) Leahy, Kwok, and Arquilla 1987. (3) Likkell *et al.* 1987. (4) Arquilla, Leahy, and Kwok 1986. (5) Nguyen *et al.* 1987. (6) Knapp *et al.* 1982; Knapp and Morris 1985; Knapp 1986. (7) Wannier and Sahai 1986. (8) Olofsson, Eriksson, and Gustafsson 1987.

diagram (Fig. 2a). Approximately half of the class 40 sources have excesses at 60 μm and are generally located above the blackbody line, similar in color to visual carbon stars. We will designate this group as class A objects. The other half of the class 40 sources are distributed along or below the blackbody line and will be designated as class B objects.

In the 25/60/100 μm color-color diagram (Fig. 2b), one will notice that the color distribution of objects is not as clearly

defined as in Figure 2a. The separation of the two classes by the blackbody line can still be seen. For comparison, the main group of class 20 objects with good photometric fluxes in all four *IRAS* bands is found to lie below class 40 objects, with a few class 20 objects found in the area of the class 40 objects.

Figures 3a and 3b show the color-color diagram of 137 radio CO stars which have good photometric measurements at all four bands. These 137 objects break down as follows: eight in

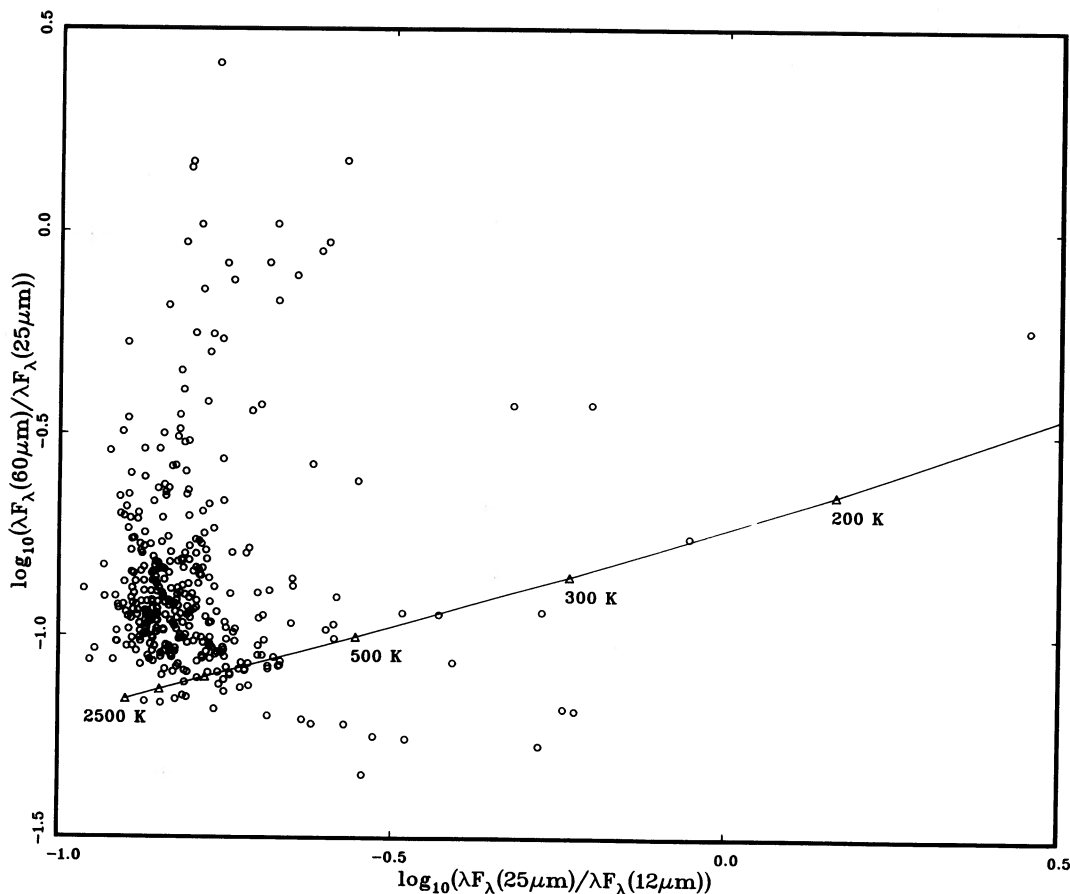


FIG. 1a

FIG. 1.—(a) The 12/25/60 μm color-color diagram of 369 visual carbon stars with good photometric fluxes in the *IRAS* 12, 25, and 60 μm bands. (b) The 25/60/100 μm color-color diagram of 91 visual carbon stars with good photometric fluxes in all four *IRAS* bands.

class 00, six in class 10, 47 in class 20, three in class 30, 47 in class 40, one in class 50, one in class 60, three in class 70, one in class 90, and 20 with no LRS classification. Comparison of Figures 2a and 3a shows that the radio CO stars have color distributions similar to that of the class B class 40 objects. About 13 objects have very low color temperatures ($T = 150\text{--}300$ K). Another five objects have very large (>0.5 dex) 25 $\mu\text{m}/12$ μm excesses. Three of the five are located below the blackbody line: they are 17436+5003 (HD 161796), 19114+0002 (SAO 124414), and 19475+3119. All three have been suggested by Volk and Kwok (1988b) as candidates for proto-planetary nebulae. The other two objects, which lie above the blackbody line, are 17103-3702 (NGC 6302, a planetary nebula), and 07399-1435 (OH 231.8+4.2, LRS type 79).

In the 25/60/100 μm color-color diagram (Fig. 3b), most of the radio CO stars lie below the blackbody line, probably as the result of decreasing dust opacity with increasing wavelength. In contrast, most of the class 40 objects and visual carbon stars have 100 μm excesses.

Comparison of the color-color diagrams (Figs. 1-3) suggest that two classes of carbon stars can be distinguished. Stars of one (class A) have relatively little circumstellar extinction and consequently are relatively bright in the visible. These stars tend to have large 60 μm excesses and are generally not radio CO-emitters. Stars of the other group (class B), which is dominated by radio carbon stars, have low color temperatures and

probably thick circumstellar envelopes. The infrared carbon stars are a mixture of the two classes.

IV. GALACTIC DISTRIBUTIONS OF VISUAL, INFRARED, AND RADIO CARBON STARS

Habing *et al.* (1985) have shown that the later-type star population in the *IRAS Point Source Catalog* exhibits a very prominent Galactic bulge. In comparison, the Galactic distribution of all sources in the LRSC fails to show the Galactic bulge. The most natural explanation is that the stars in the LRSC belong to a relatively local population. Comparison of the 12 μm flux values (~ 4 Jy) of bulge stars with the limiting 12 μm flux (~ 10 Jy) that allows a source to be admitted to the LRSC suggests that the LRSC sources are limited to within a distance of 5-6 kpc. Figure 4 shows the Galactic distribution of the class 40 objects. One can see that almost all of the class 40 objects are located between the Galactic latitudes $\pm 11^\circ$. The mean Galactic latitude $\langle b \rangle$ is 6.7 ± 0.4 . This suggests that the class 40 carbon stars are likely to be Population I objects.

Comparison of the Galactic distribution of visual carbon stars (Fig. 5) with that of class 40 objects suggests that the former is less concentrated on the plane. This, however, can be purely a distance effect. Since the visual carbon stars generally have smaller infrared excesses than class 40 objects, the requirement of three good *IRAS* fluxes may have excluded the more distant members of the visual carbon stars. Our model

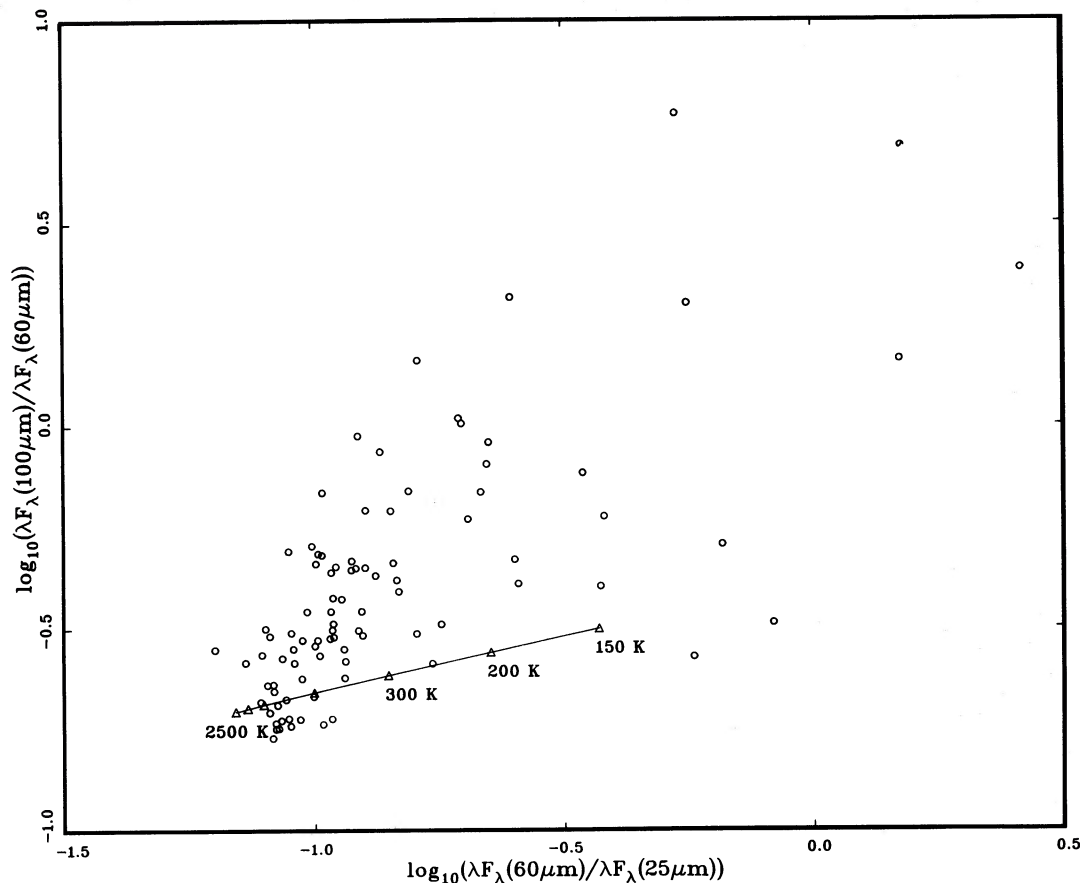


FIG. 1b

results in § VII suggest that most of the objects in this group have distances < 3 kpc.

The Galactic distribution of the CO emission objects (Fig. 6) does not show a strong concentration to the plane. An obvious inference is that they represent a relatively local population. In the table of CO-emitting stars observed by Knapp and Morris (1985), the average distance of detected objects is ~ 800 pc. Most of the more distant (> 2 kpc) objects in the radio sample are recently detected *IRAS* class 40 sources (Leahy, Kwok, and Arquilla 1987; Nguyen *et al.* 1987).

V. TRANSITION FROM M TO C STARS

The existence of two separate composition groups (oxygen-rich and carbon-rich) among AGB stars has been a long-standing puzzle in the theory of stellar evolution. Iben and Renzini (1983) suggest that the transition from M to S and then to C occurs with a time scale of about 10^5 yr during AGB evolution as the [O]/[C] abundance ratio changes gradually as the result of several dredge-up and envelope processes (Iben and Renzini 1983; Renzini and Voli 1981). Little-Marenin (1986) and Willems and de Jong (1986) find several visual carbon stars which appear to have a strong $10 \mu\text{m}$ silicate emission feature. Little-Marenin suggests that they might be in binary systems with an M- and a C-star component, whereas Willems and de Jong (1988) interpret the presence of the silicate feature as evidence of M stars in transition to C stars. From the color of these objects, they also concluded that the transition time from oxygen-rich Mira to carbon-rich Mira is of the order of 10^4 yr.

Willems and de Jong (1988) proposes the following scenario for carbon star evolution. First, an oxygen-rich circumstellar shell is formed when a star is pulsating as a Mira variable. The dust shell shows $9.7 \mu\text{m}$ silicate emission, as is characteristic of oxygen-rich stars. The mass-loss rate is about $10^{-6} M_{\odot} \text{ yr}^{-1}$ in this phase. Later, carbon becomes more abundant than oxygen in the atmosphere of the star because of the thermal pulse process. This in turn causes the star to become an irregular pulsator, and the mass-loss rate decreases sharply as compared with the Mira variable. Since almost no new dust is formed, the O-rich shell continues to expand with constant speed. After the O-rich shell moves out, a new carbon-rich circumstellar shell builds up. First an extended photosphere with polyatomic carbon molecules is formed, and then silicon carbide dust condenses; later, amorphous carbon dust condenses.

During the period after the O-rich envelope has expanded away from the star and before the C-rich envelope is formed, the central star will be surrounded by an extended dust shell detached from the star. Assuming that the dust envelope is geometrically thin and is heated by a central star of temperature T_* , then the dust temperature (T_d) is given by

$$T_d = (R_*/2R_s)^{2/5} T_*, \quad (1)$$

where the dust shell radius R_s is assumed to be much greater than the stellar radius R_* , and the dust opacity has a wavelength dependence of λ^{-1} . The optical depth of the shell (τ_λ) can be shown to be

$$\tau_\lambda = (3/16\pi)(\psi/\rho_d)(Q_\lambda/a)(\Delta M/\pi R_s^2), \quad (2)$$

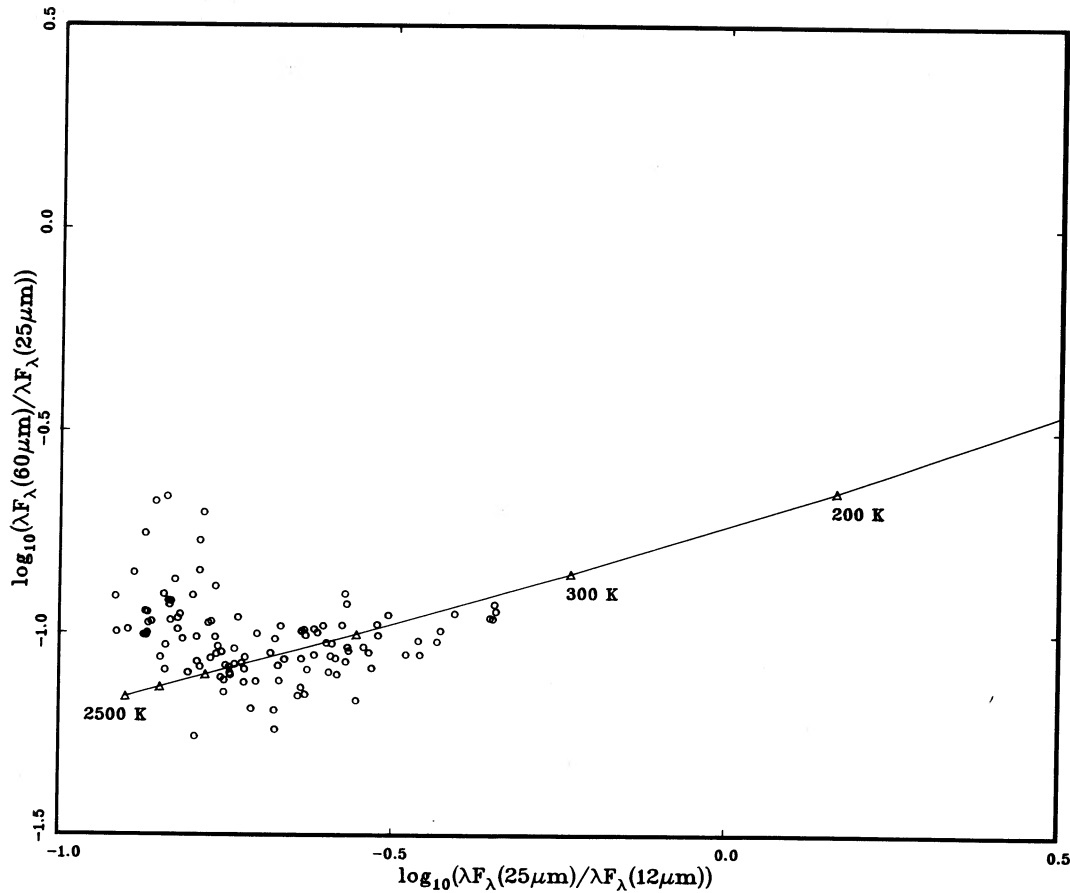


FIG. 2a

FIG. 2.—(a, b) Color-color diagrams of 111 class 40 objects with good photometric fluxes in all four of the *IRAS* bands

where ΔM is the mass of the dust shell, ψ is the dust-to-gas ratio, ρ_d is the specific gravity of the grain, a is the radius of the grain, and $\pi a^2 Q_\lambda$ is the grain absorption cross section. Assuming $\psi = 0.01$, $(Q_\lambda/a) = 2(1/\lambda) \mu\text{m}^{-1}$, and $\rho_d = 3 \text{ g cm}^{-3}$ (Willems and de Jong 1988), equation (2) then gives

$$\tau_\lambda = 12.5 \Delta M / [\lambda (\mu\text{m}) \pi R_s^2]. \quad (3)$$

Since the dust shell is of uniform temperature, the emergent spectrum is simply given by

$$F_\lambda = [\pi R_*^2 B_\lambda(T_*) e^{-\tau_\lambda} + \pi R_s^2 B_\lambda(T_d)(1 - e^{-\tau_\lambda})] / D^2, \quad (4)$$

where D is the distance.

If the dust envelope has been expanding at a constant velocity of V (assumed to be 10 km s^{-1}) since the time ($t = R_s/V$) of shell detachment, then the emergent spectrum can be calculated as a function of time. Using the above formulation, Willems and de Jong (1988) were able to derive an evolutionary track on the color-color diagram and compare the results with the colors of *IRAS* carbon stars.

Figure 7 shows the evolutionary tracks calculated following the procedure used by Willems and de Jong. The stellar temperature is assumed to be 2500 K, which, when combined with the average bolometric magnitude of Magellanic Cloud carbon stars of -4.8 (Cohen *et al.* 1981), gives a stellar radius of $R_* = 3 \times 10^{13} \text{ cm}$. The tracks are for total shell masses (ΔM) of 10^{-4} , 2.5×10^{-4} , 10^{-3} , 2.5×10^{-3} , and $10^{-2} M_\odot$. Colors of the star are calculated for $t = 40, 100, 200, 400, 1000, 2000,$

4000, and 10,000 yr since shell detachment. As the dust shell expands away from the star, the color of the object becomes redder. The tracks first move upward in the color-color diagram until the shell is so cool that it no longer dominates the spectrum. Later, the tracks turn downward in the form of a loop and converge to the blackbody line at $t \sim 10,000 \text{ yr}$. At this point, the shell is completely detached and the colors are that of the photosphere.

Also plotted on Figure 7 for comparison are 369 visual carbon stars which have good-quality *IRAS* fluxes at 12, 25, and 60 μm , and 375 class 20 objects (M stars with the 9.7 μm silicate feature in emission) with good fluxes at all four bands. It can be seen that many of the visual carbon stars have colors that coincide with those predicted by the tracks.

VI. THE MODEL

The model of Willems and de Jong (1988) assumes that the dust temperature is uniform. If the dust component is in fact the remnant of the stellar wind of a previous mass-loss episode, then we would expect a density and temperature gradient in the circumstellar envelope. They also ignore the 9.7 μm emission feature in the opacity function, although it may have a significant effect on the 12 μm *IRAS* color. Comparison of the data with the model tracks in Figure 7 shows that no silicate emission feature objects are located at the starting point of the tracks. Many of the visual carbon stars (class A sources) with large 60 μm excesses also cannot be explained by the tracks in

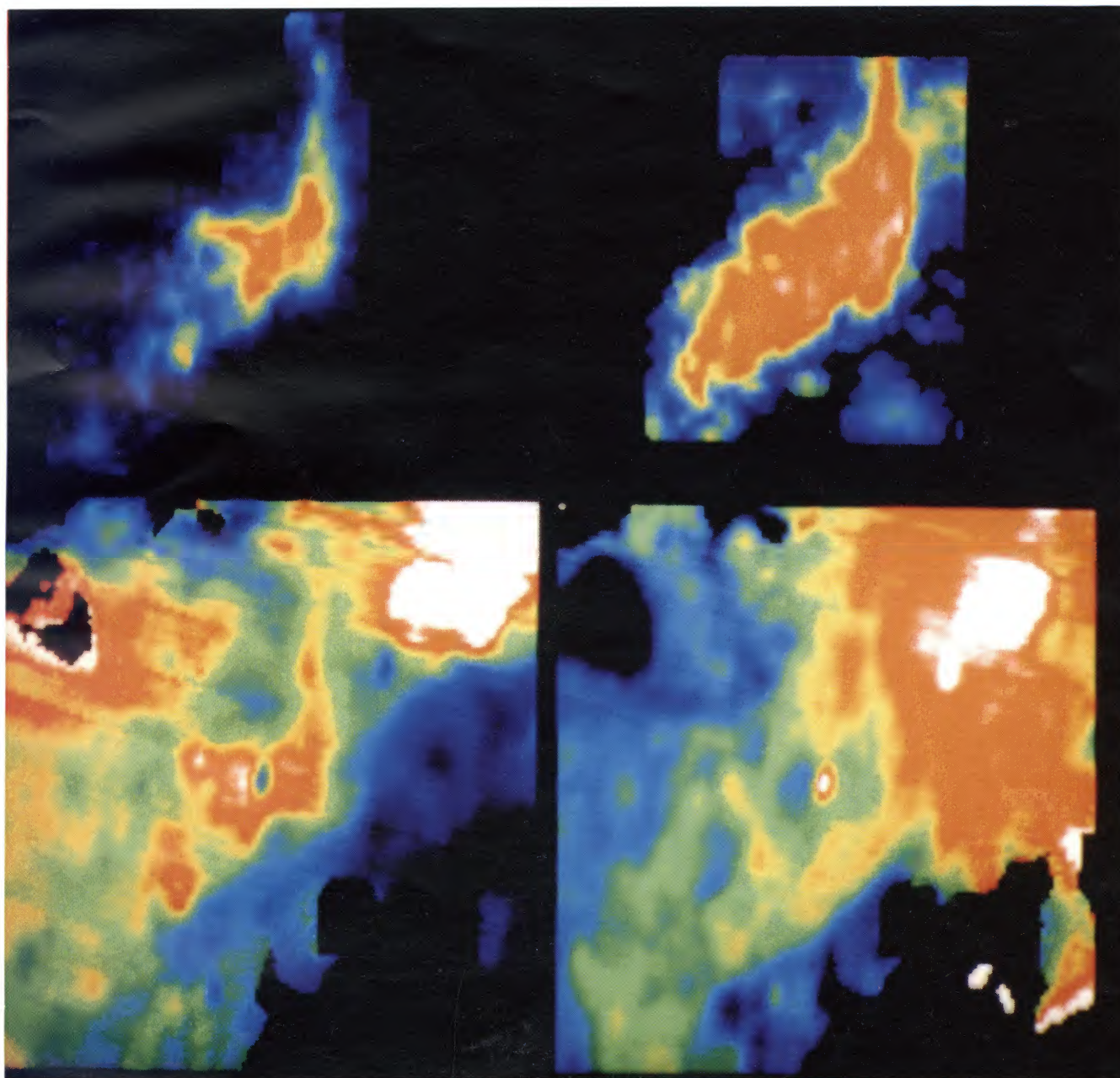


FIG. 7.—Dust optical depth (*upper left*) and temperature (*lower left*) derived from 60 and 100 μm IRAS data in the region of B5. Shown in the upper right-hand panel is the ^{13}CO integrated intensity and in the lower right-hand panel the ^{12}CO peak temperature. Molecular intensities correspond to those given in the contour maps shown in Figs. 1 and 2. There is a close resemblance between the distributions of the dust opacity and the ^{13}CO molecular column density. The dust temperature peaks are weakly anticorrelated with the gas column density; the gas temperature traced by ^{12}CO is essentially uniform over the cloud surface. In the presentation of this map, the emission of the material associated with IC 348, which would overwhelm that of B5, has been deemphasized by letting those intensities saturate the color table.

LANGER *et al.* (see 334, 368)

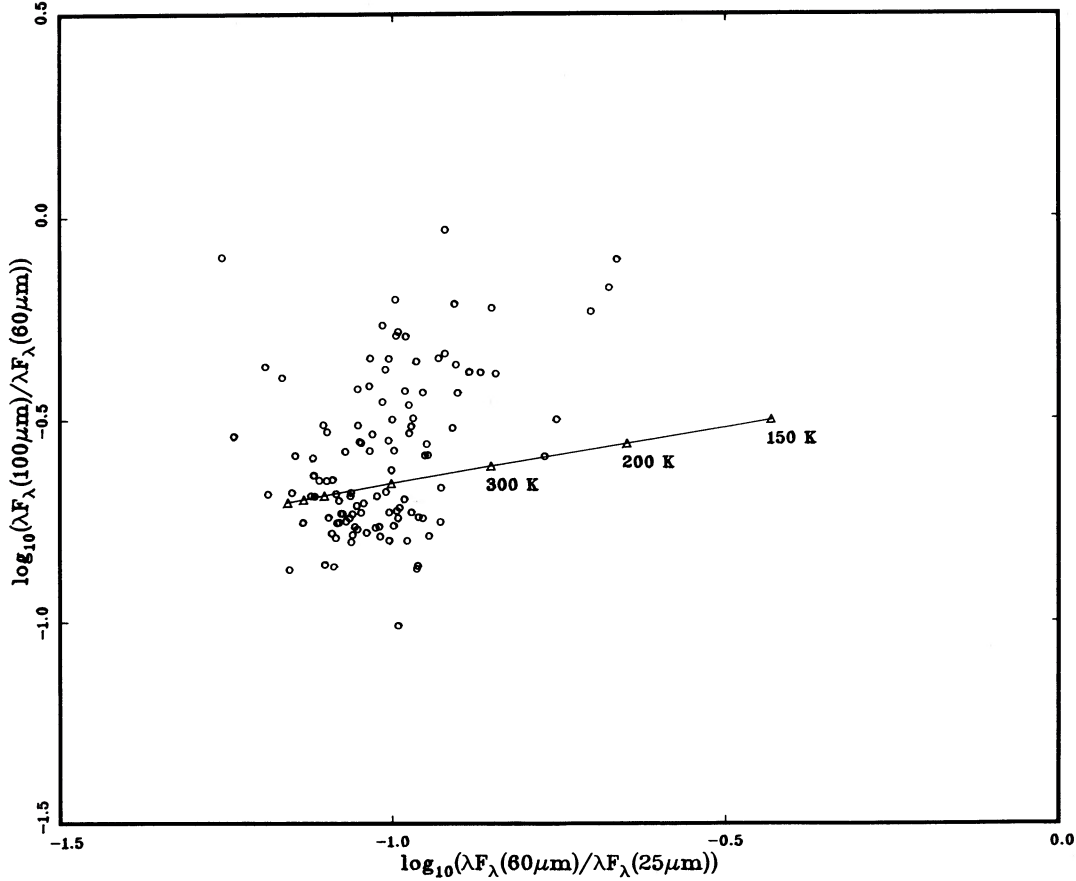


FIG. 2b

Figure 7. In order to obtain a better model, the temperature profile of the dust shell and the effect of the silicate feature on the photometric measurements have to be considered.

The dust temperature in a circumstellar environment is determined primarily by radiative processes and not by collisions. The equilibrium dust temperature is given by the balance of radiative heating from the star and thermal emission by the grain:

$$\int \sigma_{\lambda} B_{\lambda}(T_d) d\lambda = W \int \sigma_{\lambda} B_{\lambda}(T_*) d\lambda, \quad (5)$$

where $\sigma_{\lambda} = \pi a^2 Q_{\lambda}$ is the dust absorption cross section and

$$W = 0.5 \times \{1 - [1 - (R_*/r)^2]^{1/2}\} \quad (6)$$

is the dilution factor which is equal to the ratio of the solid angle subtended by the star to the total solid angle 4π . After a simple variable transformation, one obtains

$$T_d^4 F = T_*^4 W G, \quad (7)$$

where

$$F = \int \frac{\sigma_u u^3}{e^u - 1} du \quad \text{and} \quad G = \int \frac{\sigma_v v^3}{e^v - 1} dv,$$

and $u = (hc/\lambda k T_d)$ and $v = (hc/\lambda k T_*)$. F and G can be evaluated by numerical integration. Using equation (7) and a recurrent numerical interaction method, one can obtain the temperature profile.

In order to take into account the contributions of the 9.7 and

18 μm silicate features to the photometric measurements, a dust opacity function is needed. In the present model, we adopt the opacity function of Volk and Kwok (1988a), which is derived from the LRS spectra of oxygen-rich stars. For the other parameters, we use $T_* = 2500$ K, $R_* = 3 \times 10^{13}$ cm, and a dust condensation temperature of 1500 K. The combination of these parameters with the dust opacity function leads to a condensation radius (r_0) of $3.39 R_*$.

If the stellar wind velocity V is constant, then one may obtain the density profile $\rho(r)$ of the circumstellar envelope from the equation of continuity:

$$\dot{M} = 4\pi r^2 V \rho(r). \quad (8)$$

Assuming that the dust and gas are uniformly mixed and the gas-dust drift velocity is small (Kwok 1975), then the dust mass-loss rate is given by

$$\dot{M}_d = \frac{A y f}{\mu} \dot{M} = \psi \dot{M}, \quad (9)$$

where μ is the mean atomic weight of the gas per hydrogen atom, A is the molecular weight of the grain material, y is the cosmic abundance of the least abundant element in the grain, and f is the fraction of that element condensed in solid form. As in § V, we assume $V = 10$ km s $^{-1}$.

The optical depth of the circumstellar envelope at some reference wavelength λ_0 is

$$\tau(\lambda_0) = \int_{r_0}^{\infty} \pi a^2 Q(\lambda_0) n_d(r) dr, \quad (10)$$

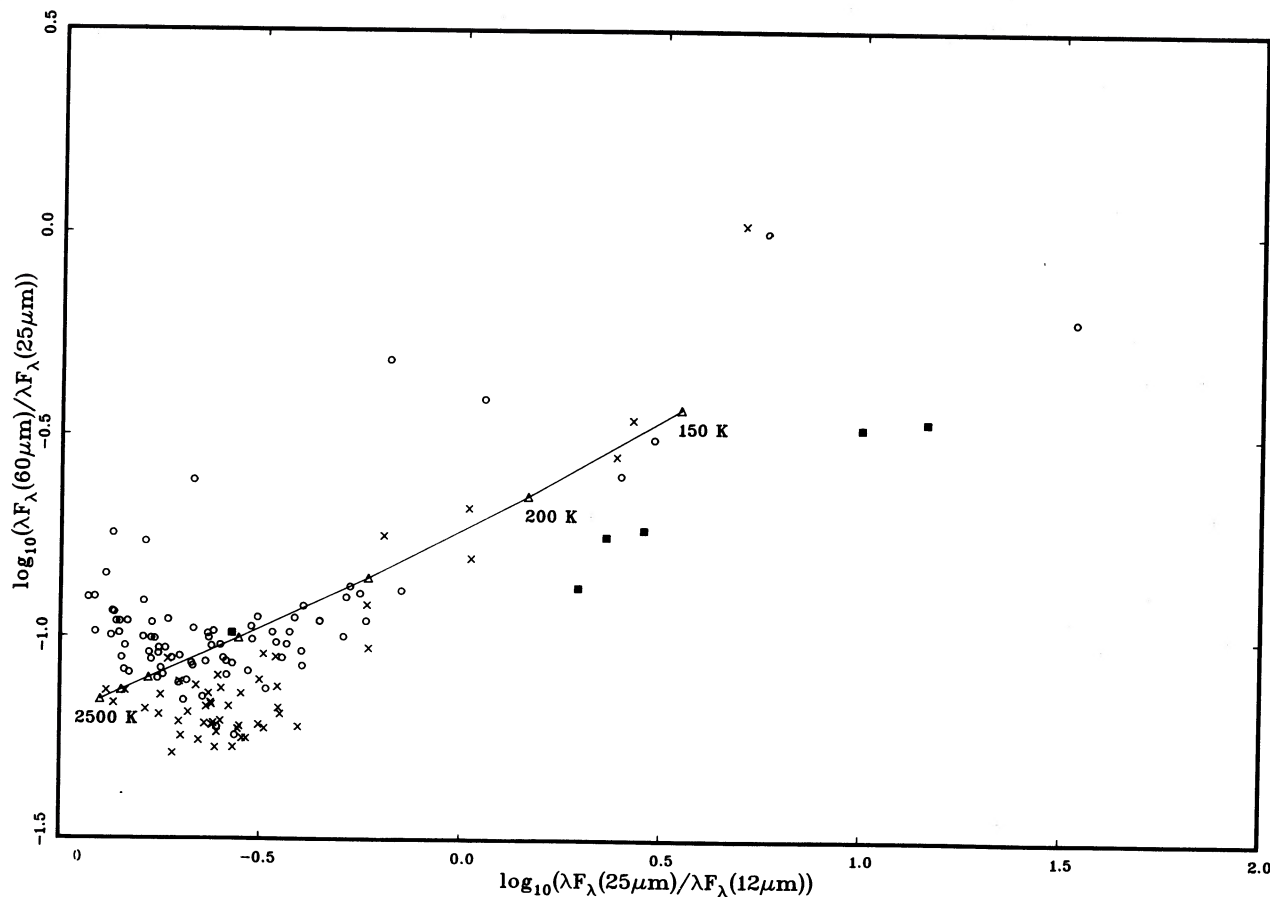


FIG. 3a

FIG. 3.—(a, b) Color-color diagrams of 137 CO emission objects with good photometric fluxes in all four IRAS bands. Crosses represent oxygen-rich stars, filled squares F, G, and K stars, and open circles C, S, N, and R stars and stars with no known spectral types.

where n_d is the number density of the dust. Assuming an inverse-square density profile appropriate for constant mass loss in the previous Mira phase,

$$\tau_\lambda = \pi a^2 Q_\lambda n_d(r_0) r_0. \quad (11)$$

Combining equations (8)–(11), one has

$$\dot{M} = C \tau_{\lambda_0} r_0 V, \quad (12)$$

where

$$C = \left(\frac{16\pi}{3} \right) \left(\frac{\rho_d}{\psi} \right) \left(\frac{a}{Q_{\lambda_0}} \right).$$

The chemical composition of the dust is assumed to be $(\text{Mg, Fe})_2\text{SiO}_4$ (Gilman 1974), and the corresponding molecular weight A is ~ 140 amu. Since the grain condensation is likely to be limited by the abundance of silicon, the value of y is set to be 4×10^{-5} , the cosmic abundance of silicon. If one assumes $\mu = 1.3$ and $f = 1$ (complete condensation), then $\psi = 4.3 \times 10^{-3}$. By assuming $\rho_d \sim 3 \text{ g cm}^{-3}$, the only free parameter left in equation (12) is Q_{λ_0}/a . In Draine's (1985) model for astronomical silicates, Q_{λ_0}/a has a value of $\sim 1.3 \mu\text{m}^{-1}$ at $9.7 \mu\text{m}$. This value of Q_{λ_0}/a implies that the constant C has a value of $4.36 \times 10^{-3} M_\odot \text{ yr}^{-1} \text{ pc}^{-1} (\text{km s}^{-1})^{-1}$. Should different values of Q/a or ψ be adopted, the change in C would only affect the corresponding gas mass-loss rates, and the spectrum would remain unchanged.

As the dust shell expands, the inner radius (r_{in}) of the circumstellar envelope is given by $r_{\text{in}} = r_0 + Vt$, where t is the time after the mass loss has stopped. Under the optically thin assumption, the emergent flux is the sum of the emission from the dust envelope and the attenuated photospheric emission:

$$F_\lambda = \frac{\pi}{D^2} \left\{ \int_{r_{\text{in}}}^{\infty} \pi a^2 Q_\lambda B_\lambda[T_d(r)] n_d(r) r^2 dr + R_*^2 B_\lambda(T_*) e^{-\tau_\lambda} \right\}. \quad (13)$$

Substituting equation (11) in equation (13), we have

$$F_\lambda = \frac{\pi}{D^2} \left\{ \tau r_0^2 \int_x^\infty B_\lambda[T_d(x')] dx' + R_*^2 B_\lambda(T_*) e^{-\tau} \right\}, \quad (14)$$

where $x = r/r_0$.

VII. RESULTS

Twelve evolutionary tracks with different initial mass-loss rates were calculated using the formulation in § VI. Each track is made up of 35 model spectra corresponding to inner shell radii from 1 to 12,400 times the initial radius r_0 . Each of the $12 \times 35 = 420$ spectra was then converted to effective IRAS colors by numerically integrating over the filter profiles given in the *IRAS Explanatory Supplement* (1985). These results are shown in Figure 8.

Figure 8 shows the model tracks for $\tau(9.7 \mu\text{m}) = 6.959, 4.175, 2.784, 2.088, 1.392, 0.696, 0.417, 0.278, 0.209, 0.139, 0.104$, and

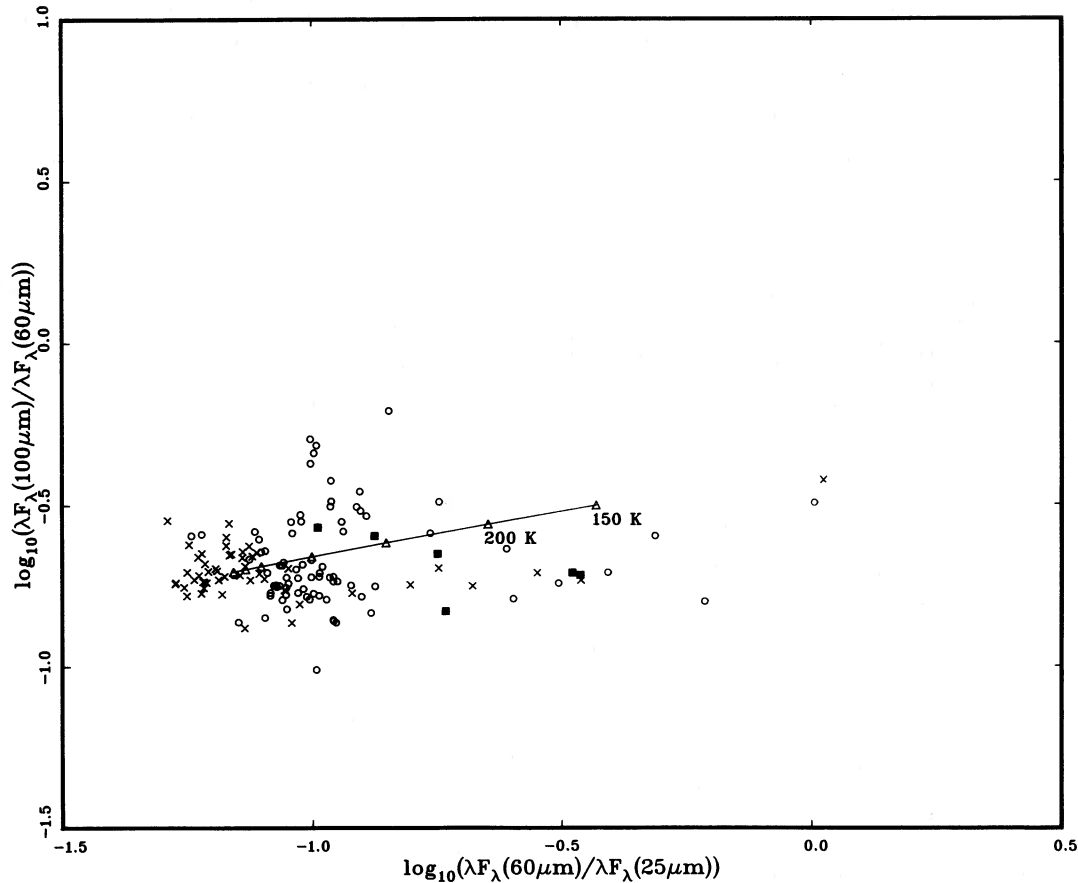


FIG. 3b

0.0696, which respectively correspond to the mass-loss rates of 1×10^{-5} , 6×10^{-6} , 4×10^{-6} , 3×10^{-6} , 2×10^{-6} , 1×10^{-6} , 6×10^{-7} , 4×10^{-7} , 3×10^{-7} , 2×10^{-7} , 1.5×10^{-7} , and $1 \times 10^{-7} M_{\odot} \text{ yr}^{-1}$. Eleven of the 35 time steps used are plotted on each track. The corresponding times for these 11 points are 0, 36, 100, 200, 400, 1000, 2000, 4000, 10,000, 2×10^4 , and 4×10^4 yr after shell detachment. We should note that for the five tracks with the highest mass-loss rates, the curve between the first and second time steps ($t = 0$ to $t = 36$ yr) are not strictly reliable because the shells are not optically thin. Also plotted on Figure 8 are the observed colors of 369 visual carbon stars in GCCCS which also have good fluxes at the *IRAS* 12, 25, and 60 μm bands, as well as 375 LRS class 20 (oxygen-rich) objects with good fluxes at all four bands. The evolutionary tracks start in the area of the color-color diagrams populated by the oxygen-rich stars and describe loops of various sizes which pass through most of the visual carbon stars. This model is particularly successful in explaining many of the carbon stars with very large 60 μm excesses. After $\sim 10^3$ yr the tracks begin to turn downward, and after $\sim 5 \times 10^4$ yr they eventually end on the blackbody line at ~ 2500 K, which is the assumed photospheric temperature. At this point, the dust shell can be considered to be completely detached.

Figure 9 shows the evolution of the spectrum of the $\tau(9.7 \mu\text{m}) = 0.417$ model as the inner radius of the shell expands from $x = 1$ to $x = 12,400$ times the initial radius. The 9.7 μm silicate feature begins prominently in emission and becomes completely unobservable at $x = 62$. The 18 μm feature is visible until $x = 310$. One can see that the peak of the dust

continuum gradually moves to longer and longer wavelength and remains detectable at $\lambda = 100 \mu\text{m}$ at $x = 12,400$. At the same time, the peak of the photospheric continuum moves to shorter wavelengths as the result of decreasing circumstellar extinction.

We have shown in Figure 8 that the model tracks are capable of explaining the color distribution of carbon stars. For some carbon stars, further observational data in the form of LRS spectra and optical and near-infrared photometry are available. It would be interesting to test the model predictions with the overall energy distributions of specific objects. These objects were selected from Figure 8 on the basis of positions coinciding with one of the model tracks. Figures 10a–10p show the spectral fits for the 62 visual carbon stars selected. Optical photometry (*UBV*) is taken from GCCCS and the *Bright Star Catalogue* (Hoffleit and Jaschek 1982), and the near-infrared photometry (*IJKL*) from Noguchi *et al.* (1981), the AFGL catalog, and the *NASA Catalog of Infrared Observations* (Gezari, Schmitz, and Mead 1984). The low point between the *K* and *L* points is a 3 μm filter designed to measure HCN and C_2H_2 absorption. No correction for interstellar extinction has been made, and this may explain the fact that the *U* points are often slightly lower than the model curve. The *IRAS* photometric measurements have been corrected for color using the procedure outlined in Kwok, Hrivnak, and Milone (1986). The model fitting parameters (τ_0 and x) are given in Table 2A. The distances of the objects given in the fifth column are derived from the fitting process.

This group of objects fitted by the model includes 16 infrared

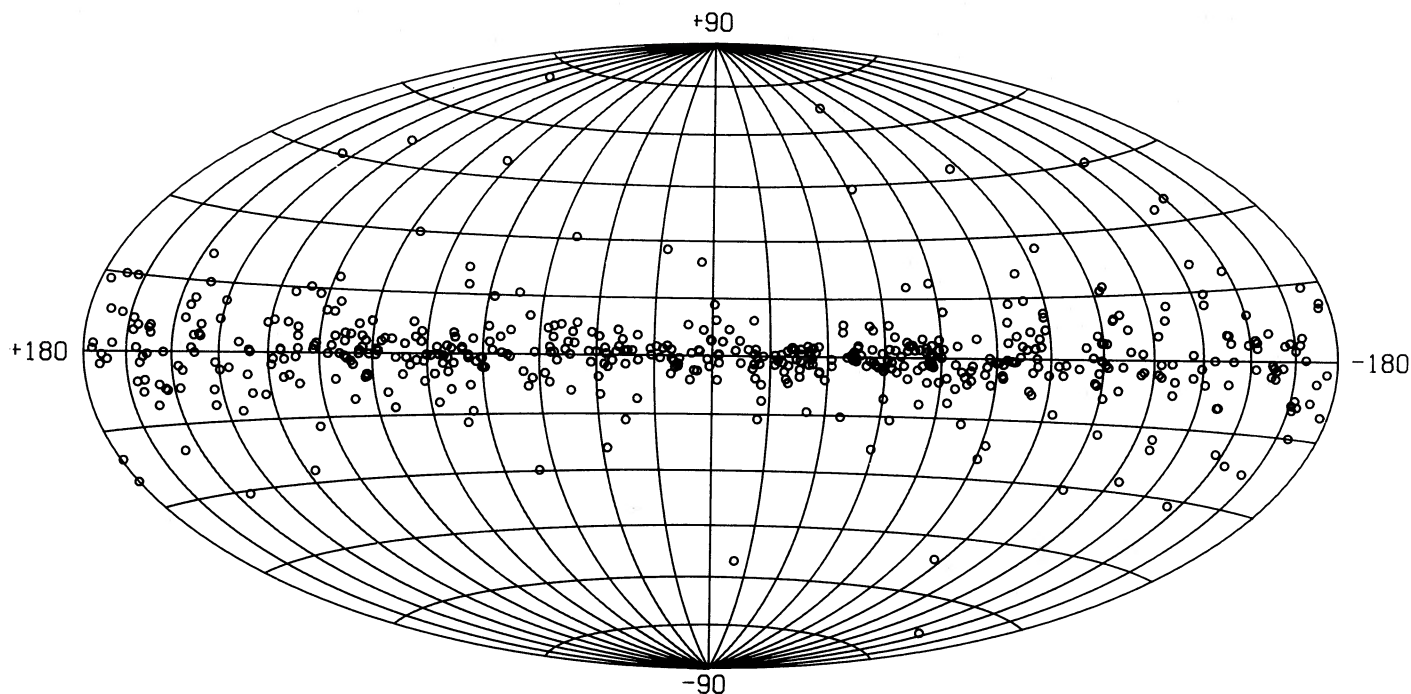


FIG. 4.—Galactic distribution of 538 class 40 objects on an Aitoff projection centered on $(l, b) = (0, 0)$. The lines of latitude and longitude are in 15° intervals.

carbon stars with the $11.2 \mu\text{m}$ silicon carbide feature (class 40 objects), two oxygen-rich stars with prominent $9.7 \mu\text{m}$ silicate features, five class 20 objects with very weak silicate features, and six class 10 objects. Thirty-three have no LRS classification. They therefore represent a range of objects which can be interpreted as stars in different stages of transition to carbon stars. The agreement between model and observations is excellent. In many cases (e.g., 05418–4628) the “kinks” in the LRS

spectra are precisely reproduced by the model. These tests give us great confidence in the correctness of the detached shell model.

We have also obtained spectral fits for another 61 objects whose spectra are less well defined because of a lack of LRS data or insufficient spectral coverage in the visible and near-infrared. The derived parameters for these 61 stars are given in Table 2B. They are on the average farther away than the 62

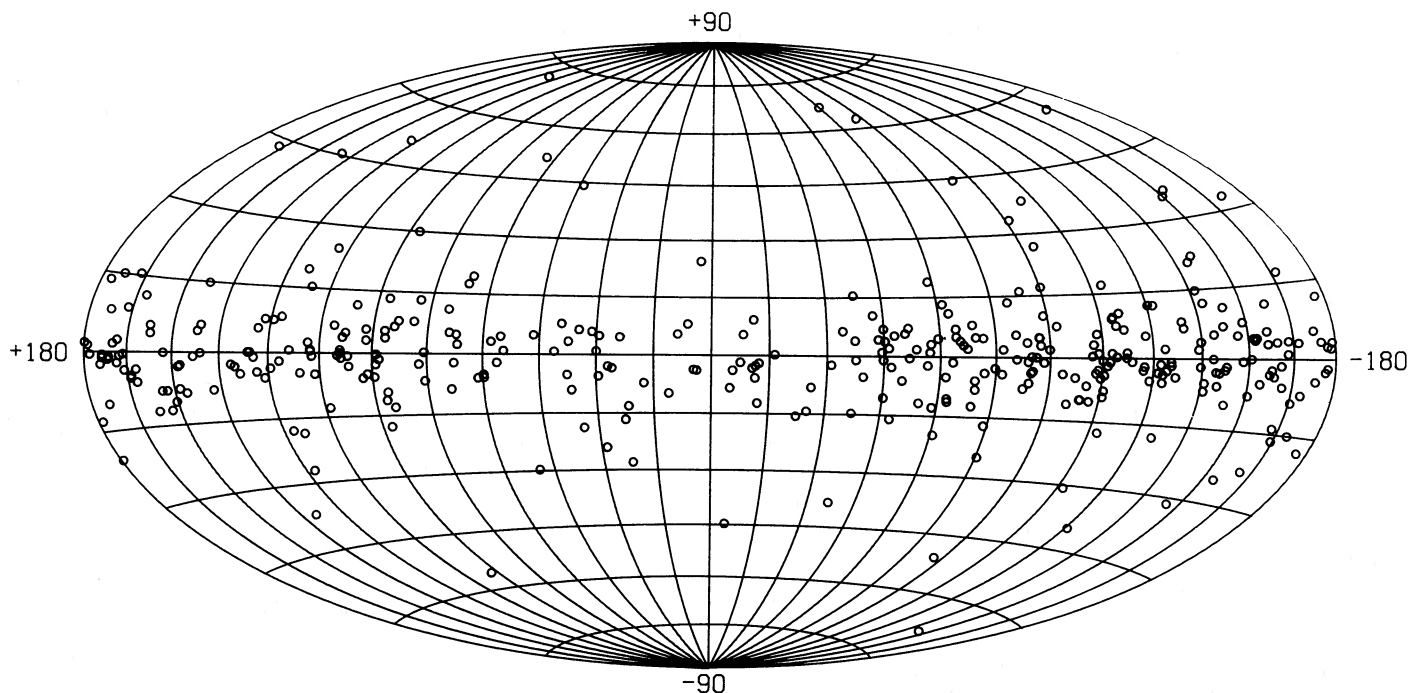


FIG. 5.—Galactic distribution of 369 visual carbon stars

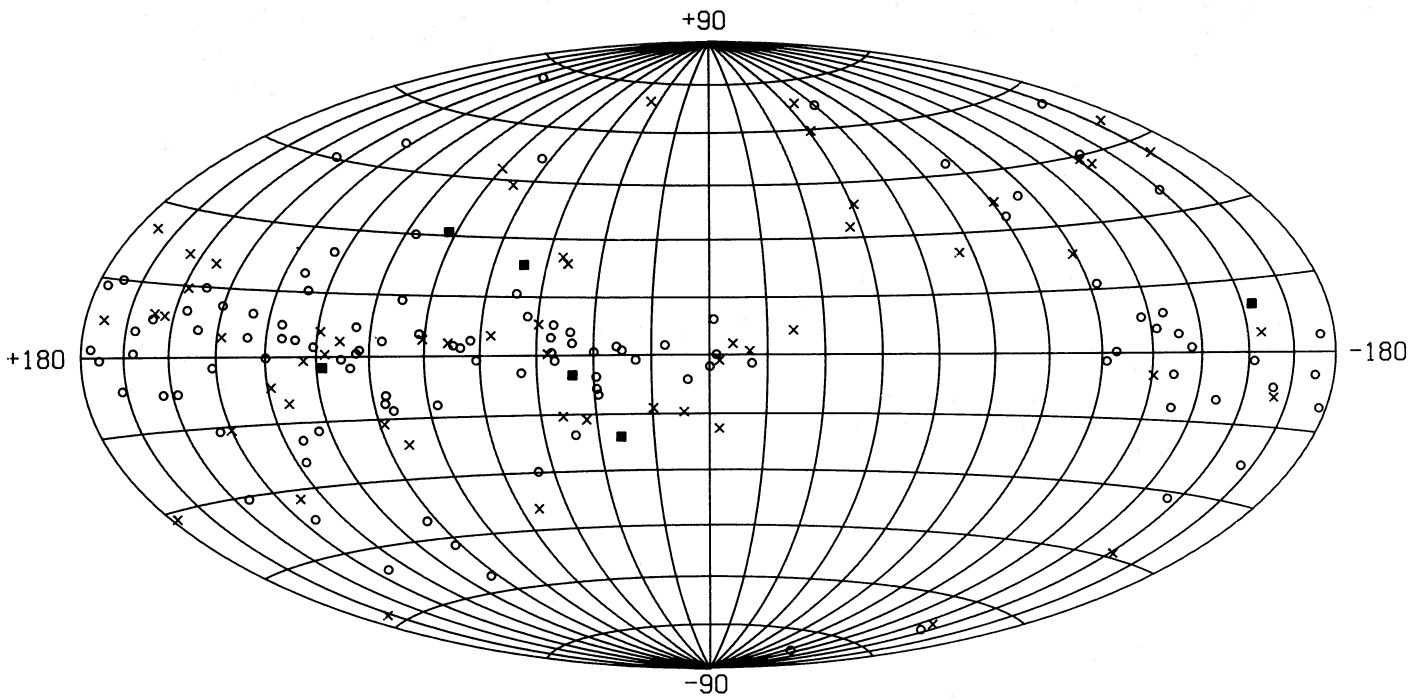


FIG. 6.—Galactic distribution of 169 CO emission objects. Crosses represent oxygen-rich stars, filled squares F, G, and K stars, and open circles C, N, R, S stars and stars with no known spectral types.

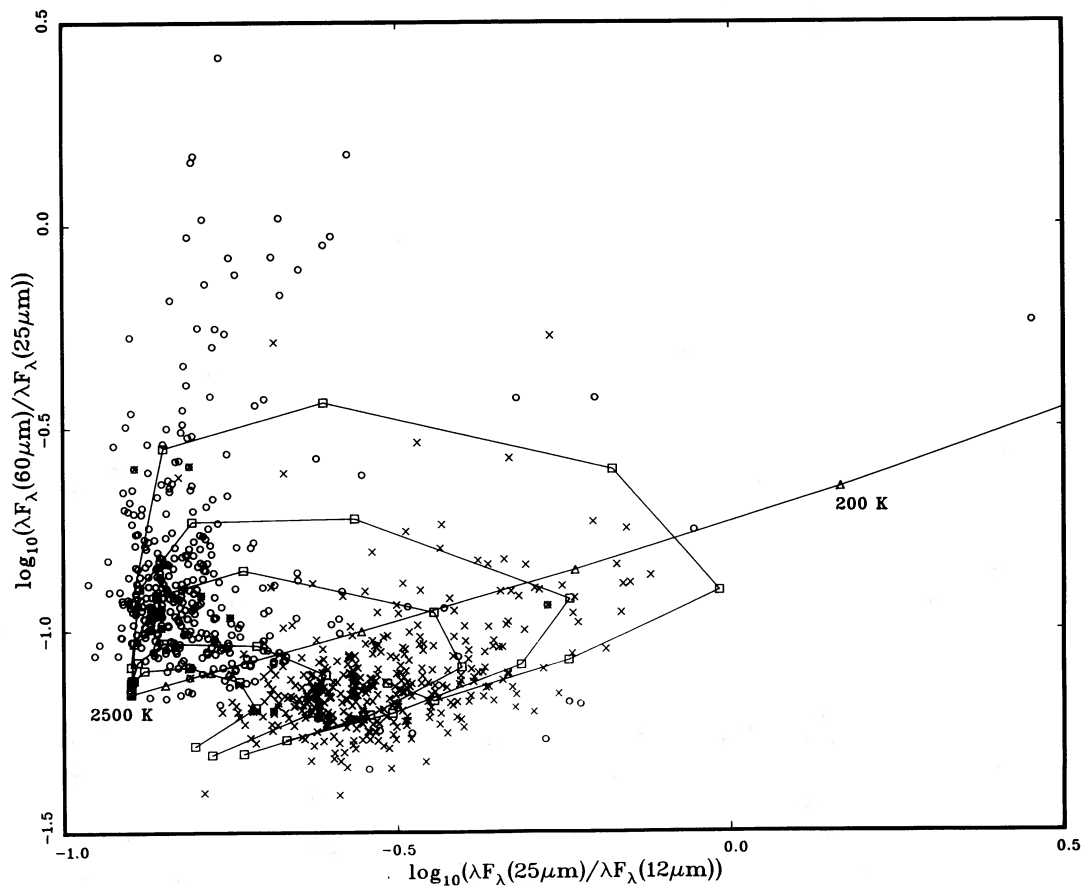


FIG. 7.—Evolutionary tracks of Willems and de Jong (1988) in the color-color diagram. Also plotted are the visual carbon stars (*open circles*) with good *IRAS* 12, 25, and 60 μm fluxes, and LRS class 20 objects (*crosses*) which have good-quality *IRAS* fluxes at all four bands. Also shown is a blackbody line with points (*triangles*) on the line representing temperatures of (from right to left) 200, 300, 500, 1000, 1500, and 2500 K. The model tracks are for shell masses of 1×10^{-4} , 2.5×10^{-4} , 1×10^{-3} , 2.5×10^{-3} , and $1 \times 10^{-2} M_{\odot}$, with ΔM increasing from the inner to the outer track. The time steps (*open squares*) on the track represent (*anticlockwise*) $t = 40, 100, 200, 400, 1000, 2000, 4000, \text{ and } 10,000$ yr.

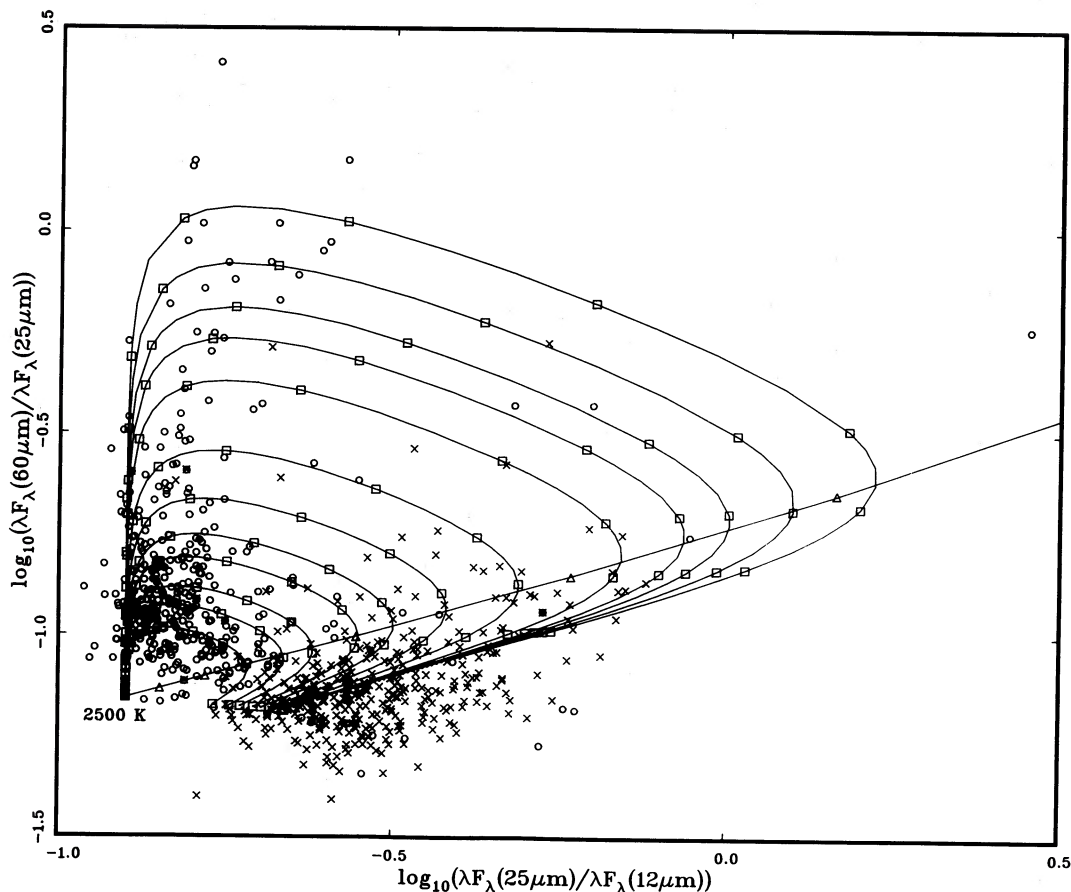


FIG. 8.—Evolutionary tracks for carbon stars on the color-color diagram. Also plotted are the visual carbon stars (*open circles*) with good *IRAS* 12, 25, and 60 μm fluxes, and LRS class 20 objects (*crosses*) which have good-quality *IRAS* fluxes at all four bands. The model tracks are for $\tau_{9.7\mu\text{m}} = 6.959$ (outermost), 4.175, 2.784, 2.088, 1.392, 0.696, 0.417, 0.278, 0.209, 0.139, 0.104, and 0.0696, which correspond to the mass-loss rates of 1×10^{-5} , 6×10^{-6} , 4×10^{-6} , 3×10^{-6} , 2×10^{-6} , 1×10^{-6} , 6×10^{-7} , 4×10^{-7} , 3×10^{-7} , 2×10^{-7} , 1.5×10^{-7} , and $1 \times 10^{-7} M_{\odot} \text{yr}^{-1}$. The time steps (*squares*) for each curve are (*anticlockwise*) 0, 36, 100, 200, 400, 1000, 2000, 4000, 10,000, 20,000, and 40,000 yr. Also shown is a blackbody curve with triangles (*starting from right*) denoting temperatures of 150, 200, 300, 500, 1000, 1500, and 2500 K.

objects in Table 2A, but are otherwise similar in nature. Most of the objects with large values of x (more detached shells) are found in the second group.

VIII. DISCUSSION

We have shown that the model evolutionary tracks can successfully explain the color distribution of carbon stars. The model spectra are also able to fit the observed far-infrared excesses in carbon stars. With our model, the initial mass-loss rate and time since shell detachment of any carbon star can be determined from its location in the color-color diagram by matching it to one of the model evolutionary tracks. In order to account for the large range of excesses observed ($\log [\lambda F_{\lambda}(60 \mu\text{m}) / \lambda F_{\lambda}(25 \mu\text{m})] = -1$ to $+0.5$), a range of mass-loss rates from 10^{-7} to $10^{-5} M_{\odot} \text{yr}^{-1}$ is needed. This 2 order of magnitude range in Mira mass-loss rates can be the result of stars entering the carbon star phase at different times on the AGB or, more probably, the result of different initial (main-sequence) masses. In our model, we have made the approximation that all AGB stars enter the carbon star phase at the same effective temperature. In reality, since stars with different initial masses begin the AGB with different core masses, it is more likely that they make the transition to carbon stars at different points on the AGB, and therefore at different effective

temperatures. However, the range of uncertainty in T_{eff} is at most a few hundred degrees. While this may have some effect on the derived parameters (τ_0 and x), we do not believe this will significantly change the results.

In our model, we also attempt to fit all carbon stars with the same luminosity. Again, different carbon star entry points on the AGB also point to a range of luminosities. For example, Frogel and Blanco (1984) have suggested that the transition luminosity increases with increasing initial mass. The only results affected in this case are the derived distances. If there is a factor of 2 range in luminosity, the error in the derived distances would be a factor of 1.4.

a) Cause of the Termination of Mass Loss

Willems and de Jong (1988) suggest that the O-rich to C-rich transition on the AGB is accompanied by a change of pulsation from Mira to non-Mira pulsation. Using the variability classes in the GCVS, the percentage of visual carbon stars which are small-amplitude variables of various types are estimated as follows: out of 313 visual carbon stars listed in the GCVS, about 76% are irregular or semiregular variables, with a breakdown of Lb-type (34%), SRa-type (8%), SRb-type (16%), and SR (12%) and other types of irregular variables (6%). About 21% are Mira variables.

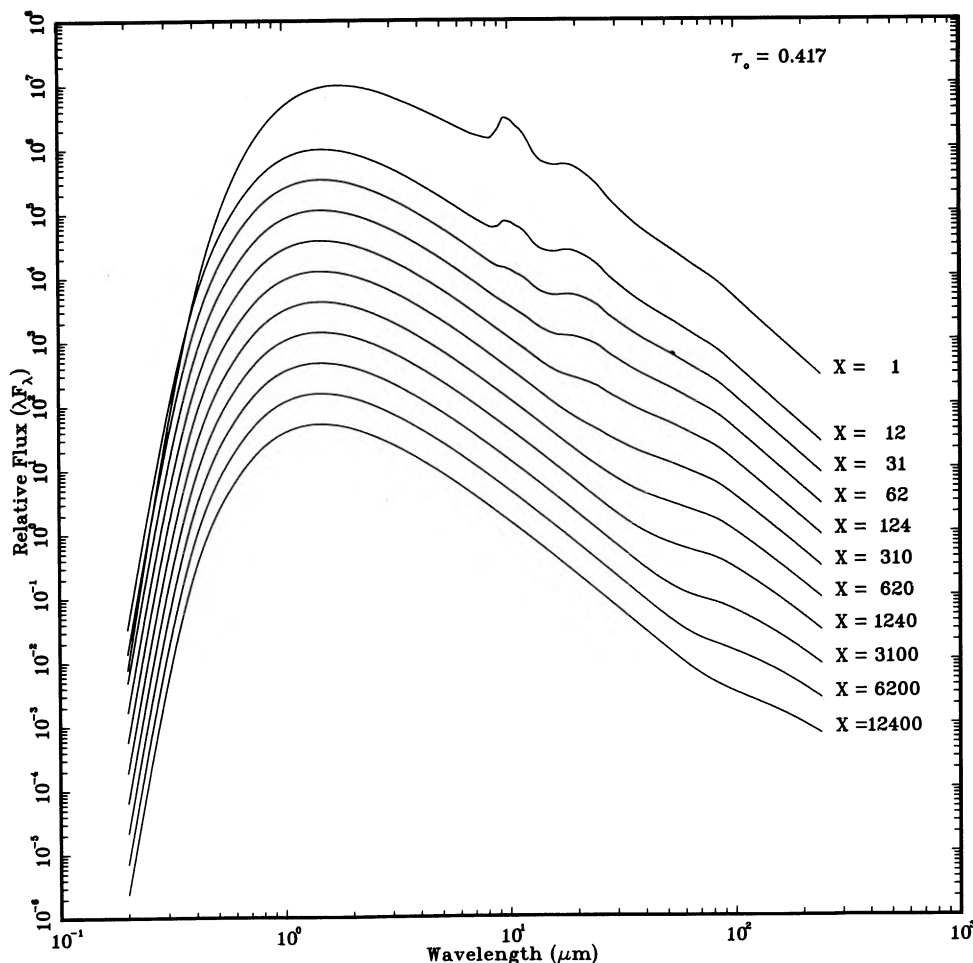


FIG. 9.—Evolution of the spectrum of the $\tau_{0.7 \mu\text{m}} = 0.417$ model from $x = 1$ to $x = 12,400$

Whether the change in pulsation behavior of the star is the cause or effect of the termination of mass-loss is still a matter of controversy. If mass-loss is driven by pulsation, it is unclear how a change in the chemical composition of the atmosphere as a result of dredge-up should have any effect on the dynamical pulsation of the atmosphere. It appears more likely that the change in the O/C ratio locks all oxygen in CO and no oxygen is available to form silicate grains. If mass loss is driven by radiation pressure on grains (Kwok 1975), then cessation of the formation of silicate grains provides a natural explanation to the sudden termination of mass-loss.

Another episode of mass loss and Mira-like pulsation will begin after (or accompanied by) the formation of carbon-based grains. The lifetime of low-amplitude pulsation is therefore approximately equal to the transition time, which is of the order of a few times 10^4 yr. Note that according to the above variability statistics, $\sim 21\%$ of the carbon stars in our *IRAS* sample have already turned into large-amplitude pulsating variables. Figure 11 shows the color distributions of the large- and small-amplitude pulsators. The large-amplitude pulsators seem to cluster more toward the blackbody line (or at a larger epoch since shell detachment), which is consistent with the suggestion above.

b) Mass-Loss Rates of the Transition Objects

The mass-loss rates of transition objects derived from this model can be compared with mass-loss rates derived from CO

observations. The most comprehensive search for CO emission from visual carbon stars is that by Olofsson, Eriksson, and Gustafsson (1987). In Table 3 we show the comparison of the mass-loss rates of eight carbon stars determined by our model fits and those derived from CO observations. The best observed carbon star is 12427+4542 (Y CVn). The mass-loss rates given by Knapp and Morris (1985), Wannier and Sahai (1986), and Olofsson, Eriksson, and Gustafsson (1987) are respectively 9×10^{-8} , $(2-4) \times 10^{-7}$, and $1.1 \times 10^{-7} M_{\odot} \text{ yr}^{-1}$. The value determined from our model is $1.5 \times 10^{-7} M_{\odot} \text{ yr}^{-1}$ ($\tau_0 = 0.104$) with an inner radius of 6.3×10^{15} cm. The agreement between these values is very good given the uncertainties in the dust-to-gas ratio (for the infrared-derived mass-loss rates) and the CO to H_2 ratio for the radio rates. The distance derived from our model is ~ 273 pc, in reasonable agreement with the distance of 350 pc given in Knapp and Morris (1985) and the distance of 280 pc given in Olofsson, Eriksson, and Gustafsson (1987).

The mass-loss rates determined for these visual carbon stars are up to 2 orders of magnitude smaller than the mass-loss rates of infrared carbon stars. This is entirely consistent with our premise that these objects are transition objects and the circumstellar envelope is created by a previous phase of mass loss. It also implies that the mass-loss rate increases dramatically after the large-scale formation of carbon-based grains. A number of the visual carbon stars detected by Olofsson, Eriksson, and Gustafsson (1987) are class 40 objects, which suggests

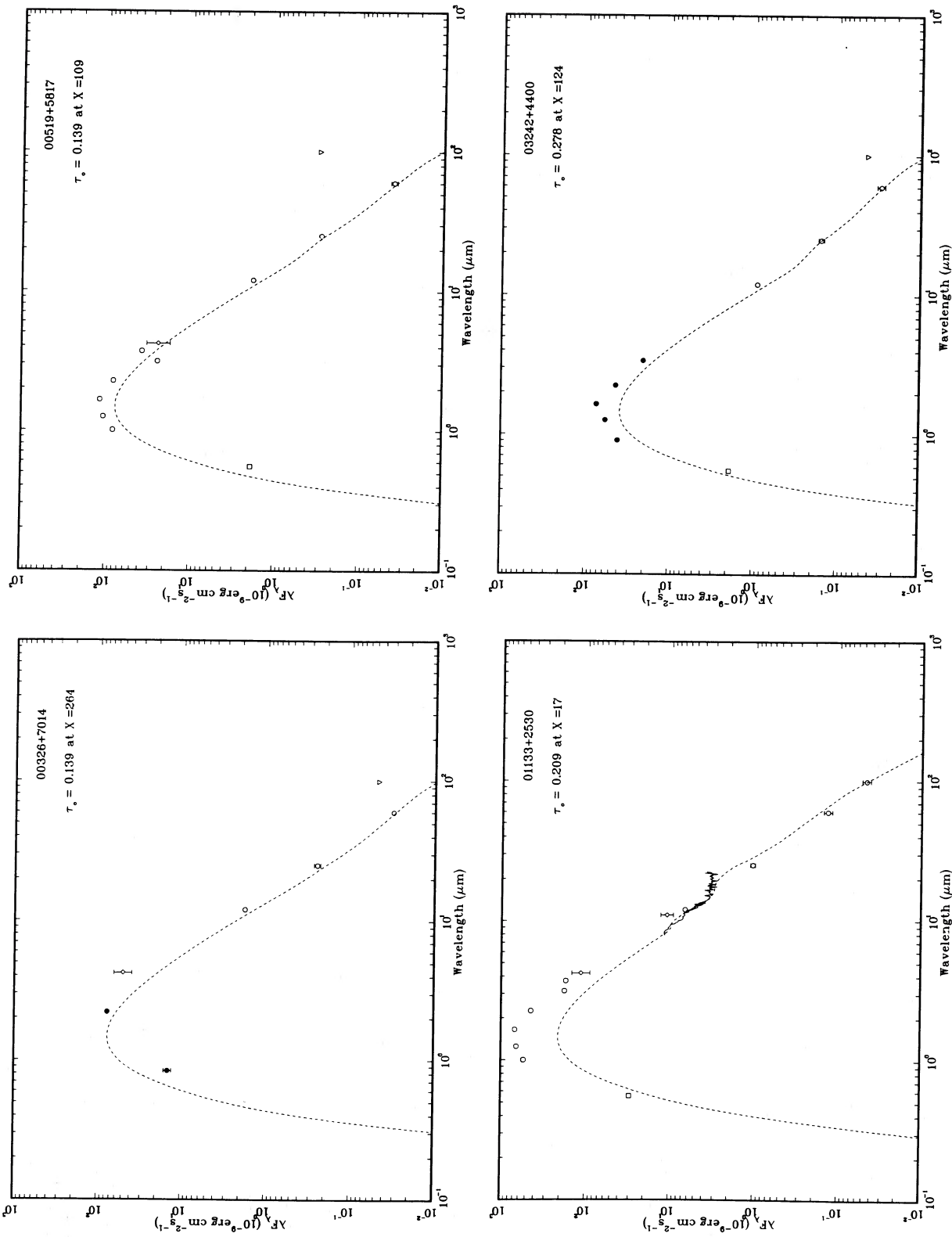


FIG. 10a

FIG. 10—(a-p) Model spectral fit for 62 visual carbon stars. The IRAS low-resolution spectra and photometry are represented by solid lines and by circles, respectively, and the filled squares are (UBV) photometry measurements taken from the *Bright Star Catalogue*. The (VJHKL) photometry measurements by Stephenson (1973) and Noguchi *et al.* (1981) are shown as open squares and hexagons, respectively. The photometry point between the K and L points is a $3 \mu\text{m}$ filter to measure absorption. Measurements listed in the AFGL catalog and the NASA *Catalog of Infrared Observations* (Gezari, Schmitz, and Mead 1984) are plotted as diamonds and filled circles, respectively. Upper limits (usually at $100 \mu\text{m}$) are denoted by triangles. The model is plotted as dashed lines. Parameters of the fits are given in Table 2A.

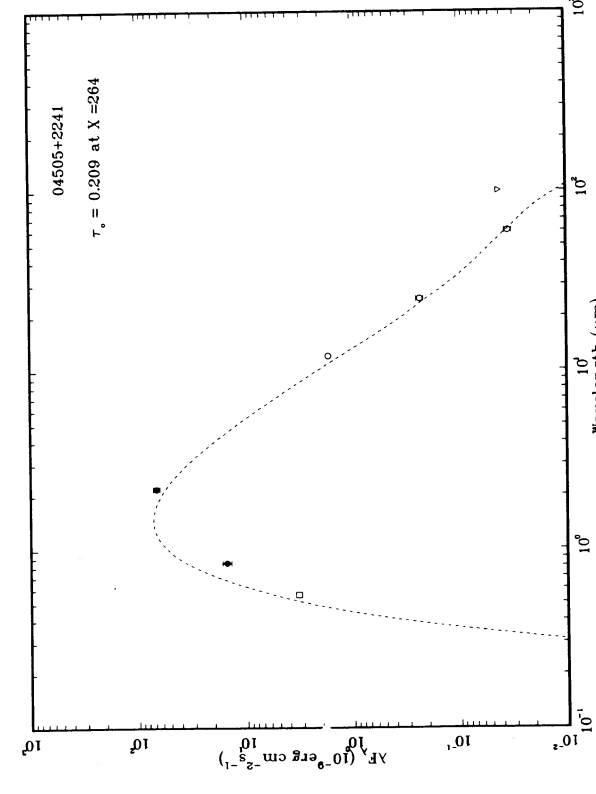
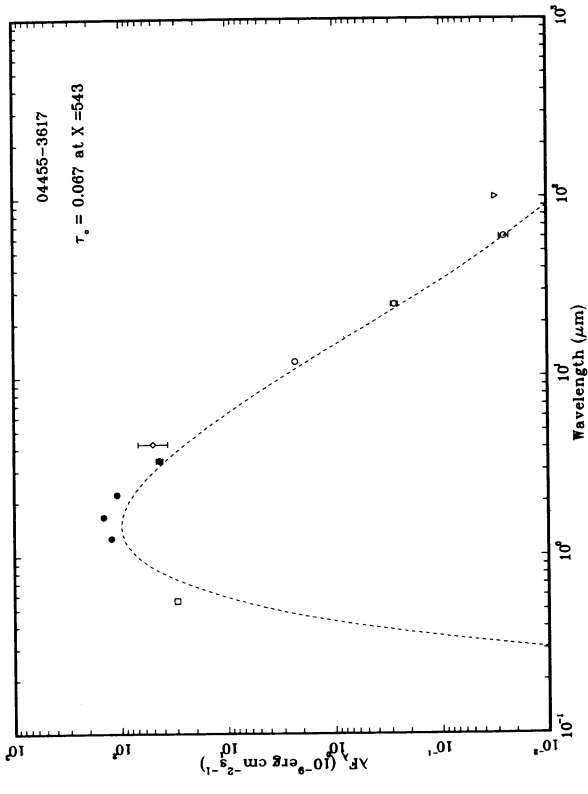
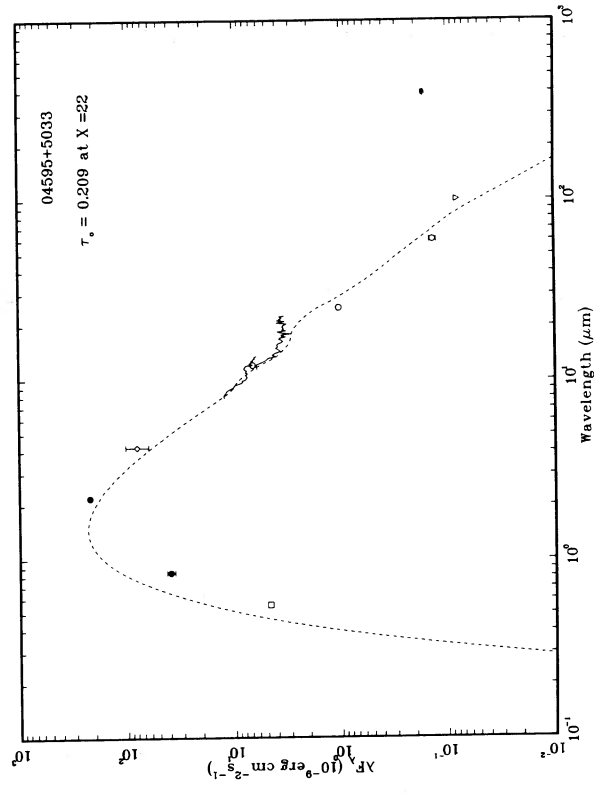
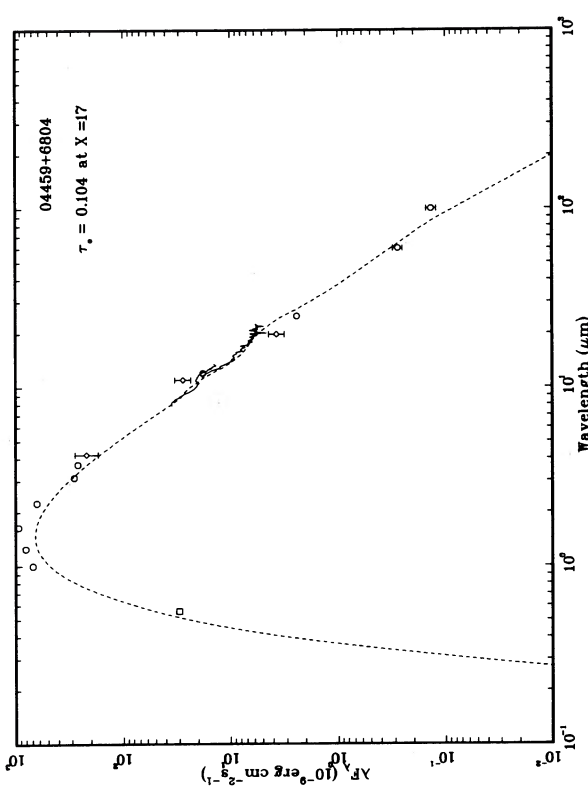


FIG. 10b

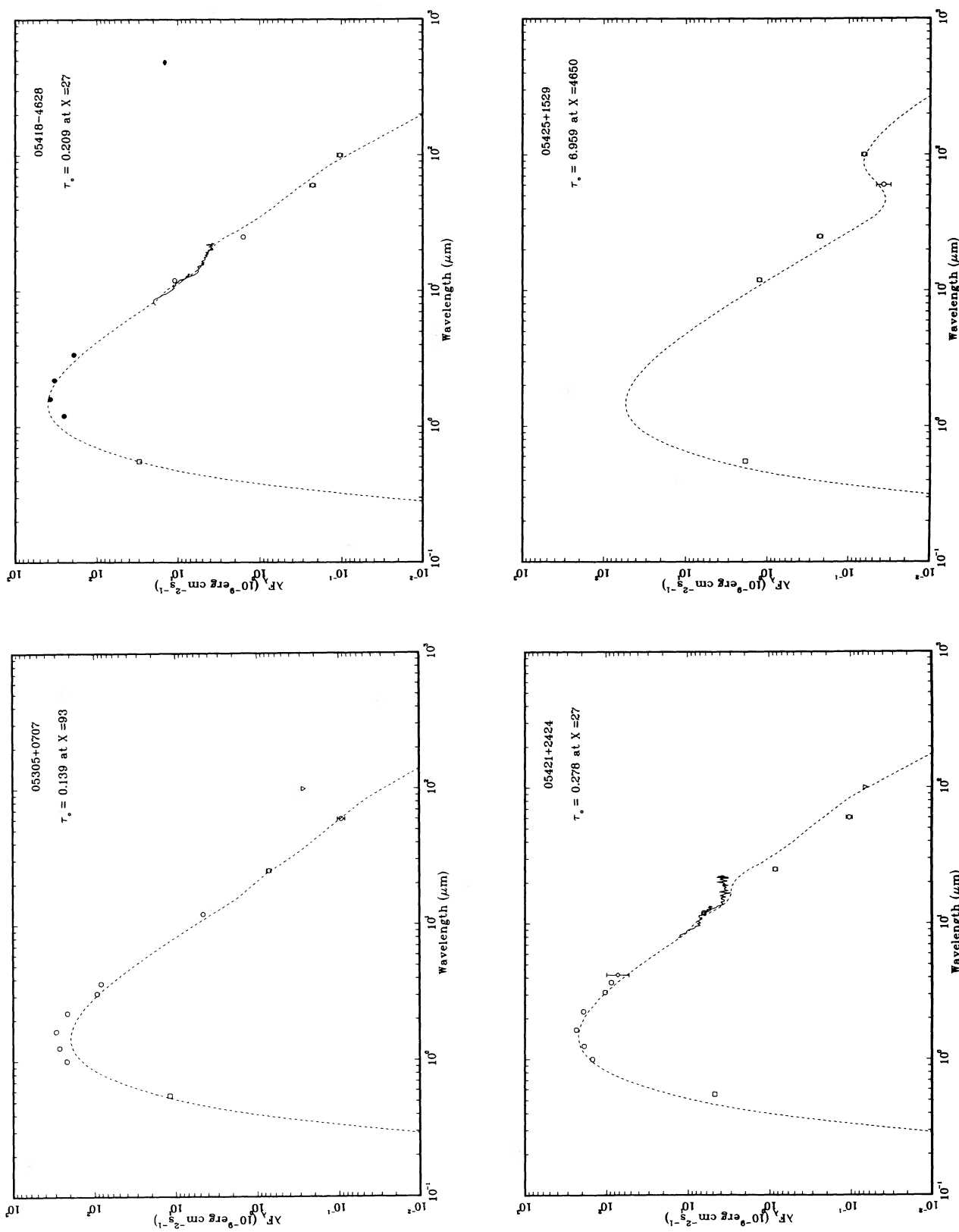


FIG. 10c

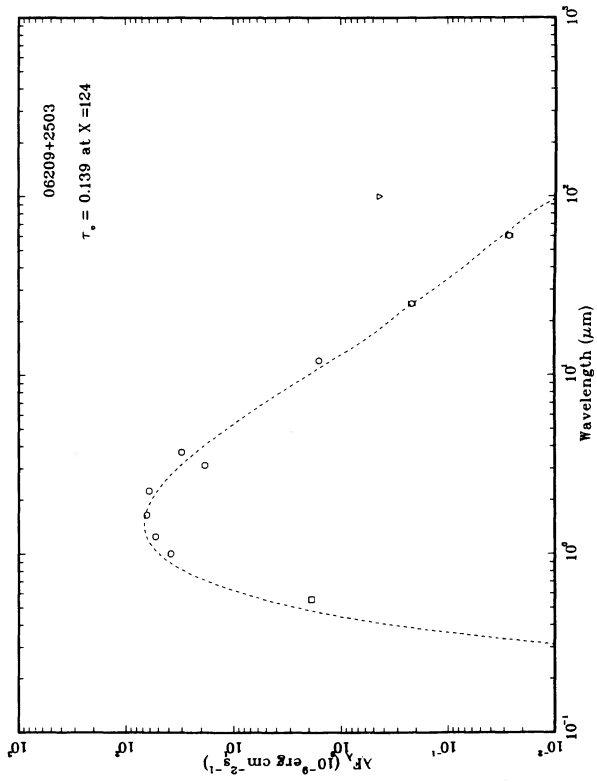
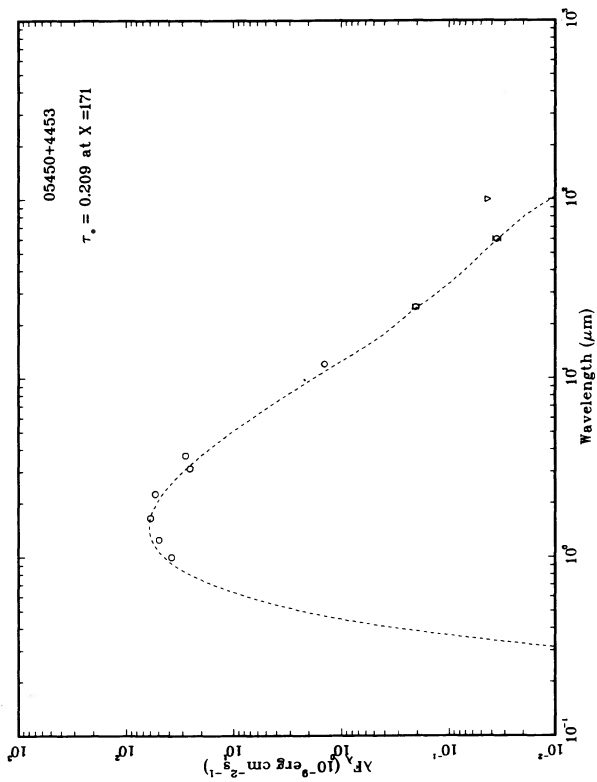
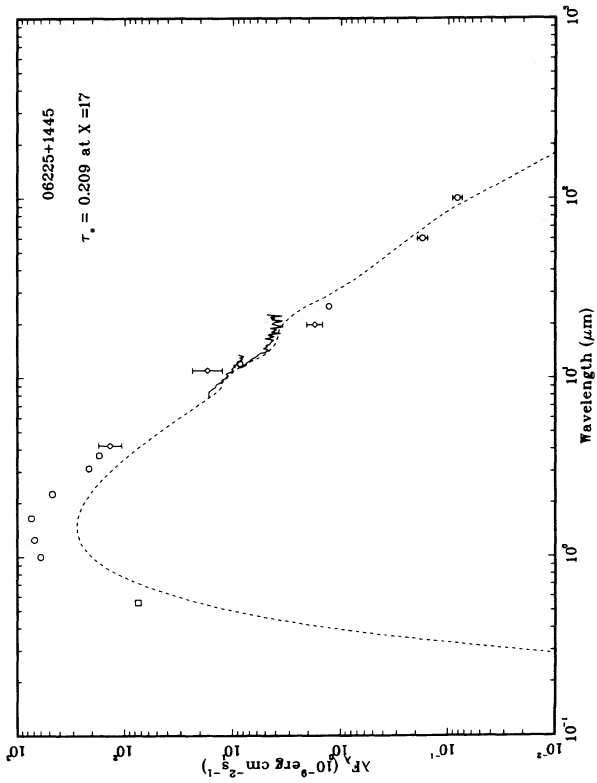
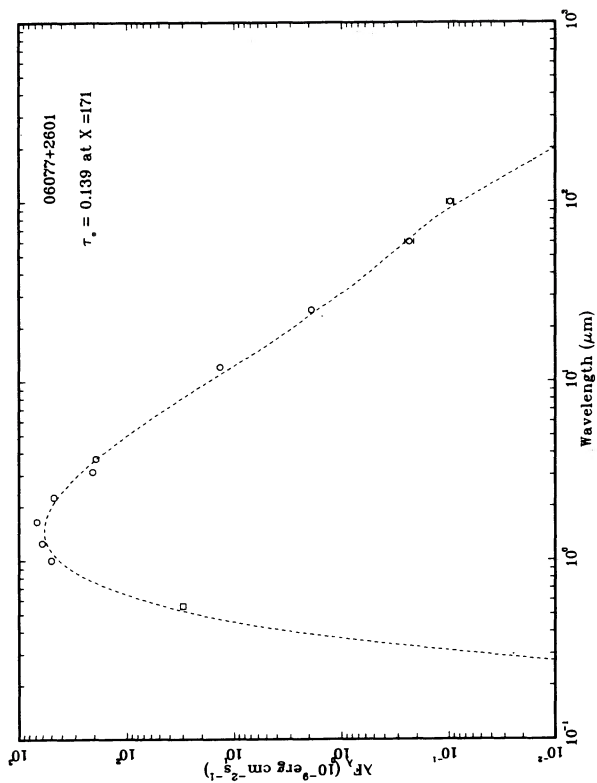


FIG. 10d

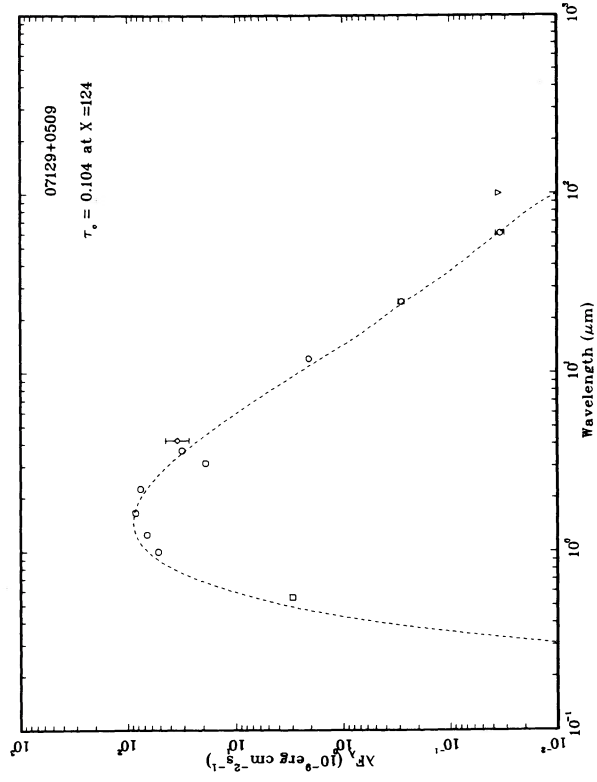
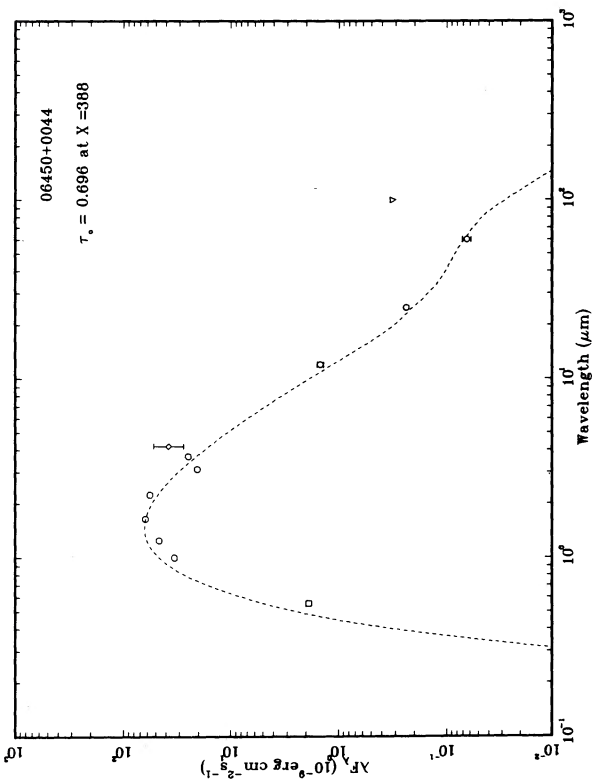
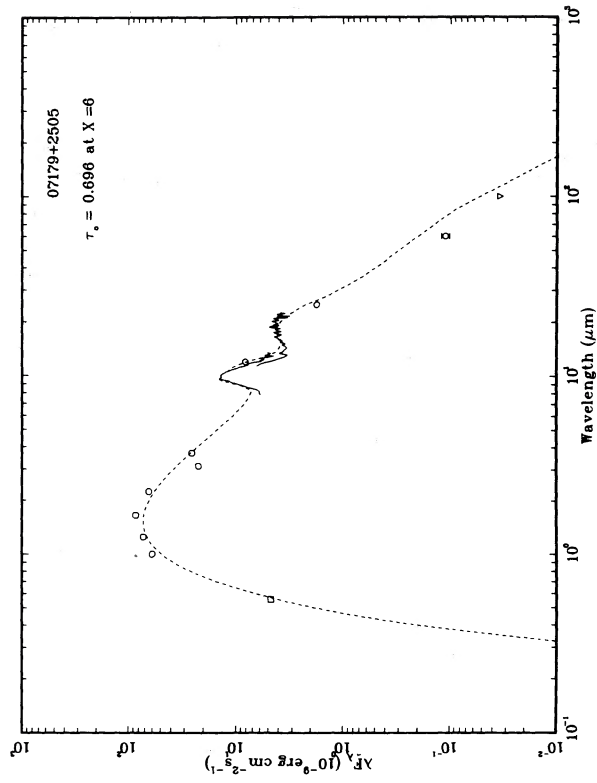
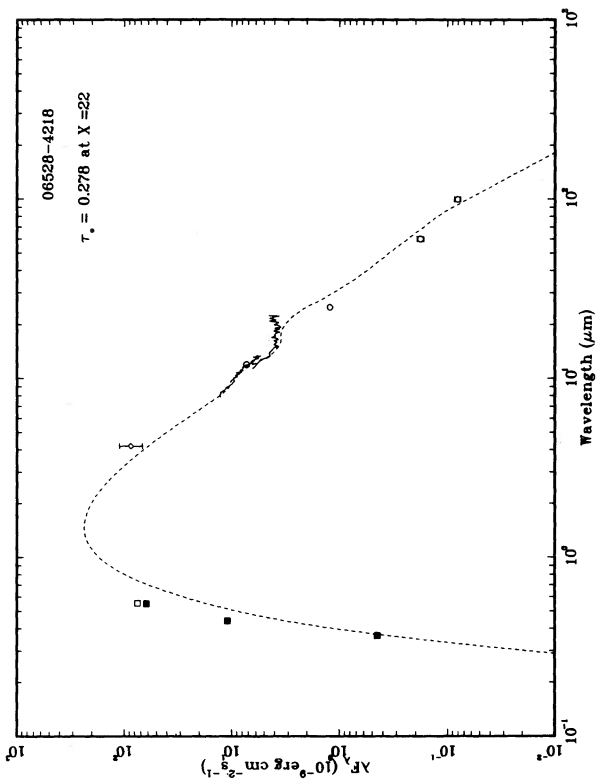


FIG. 10e

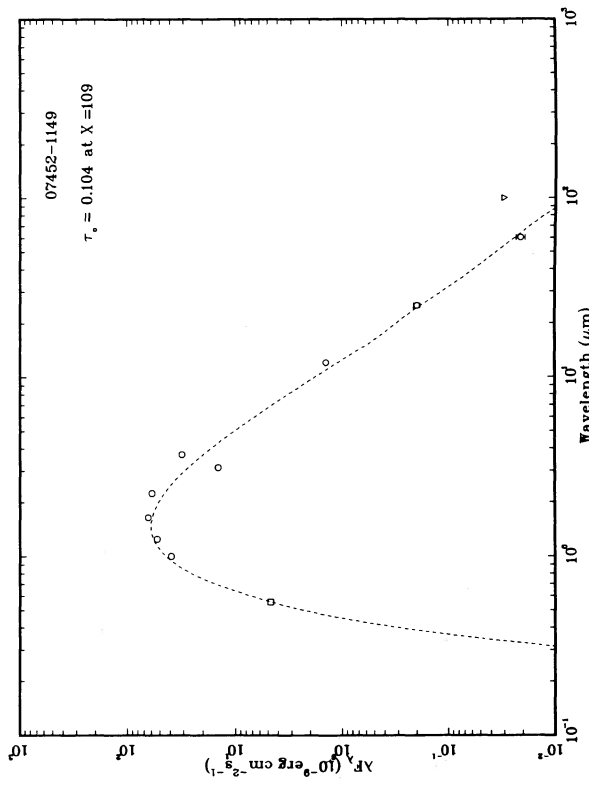
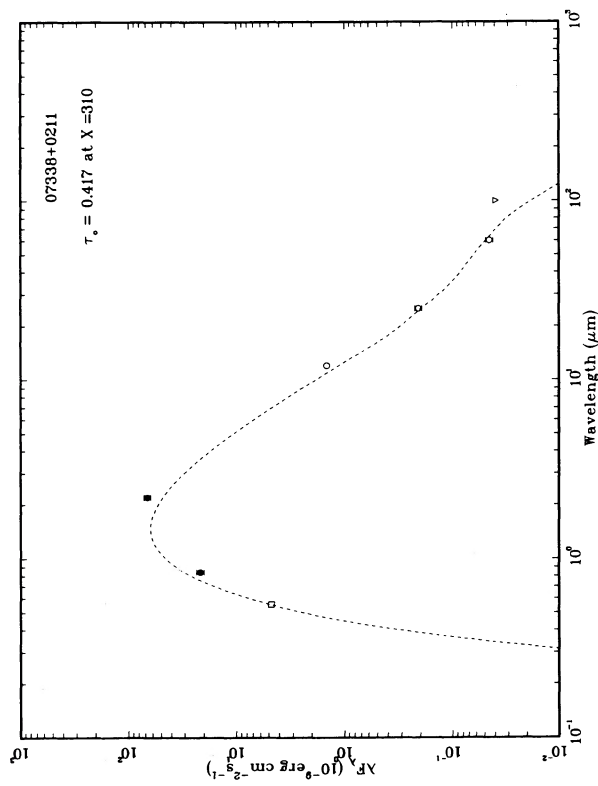
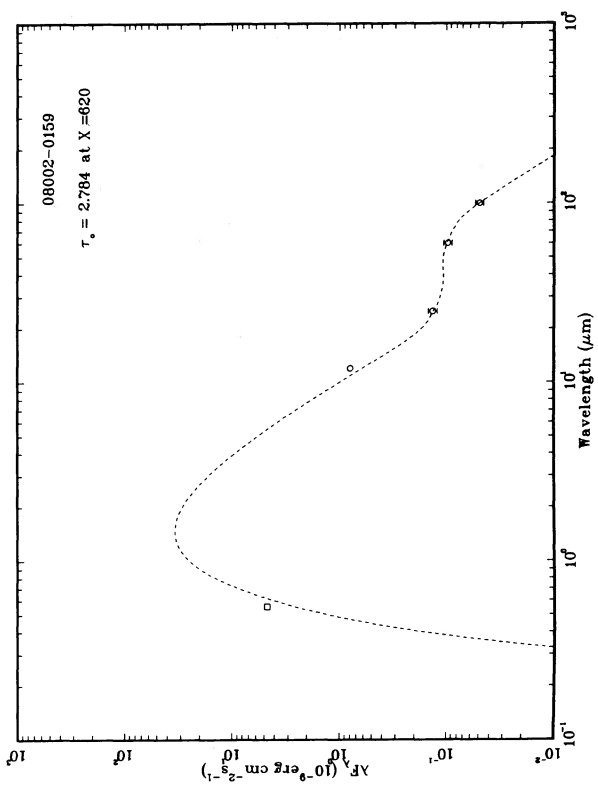
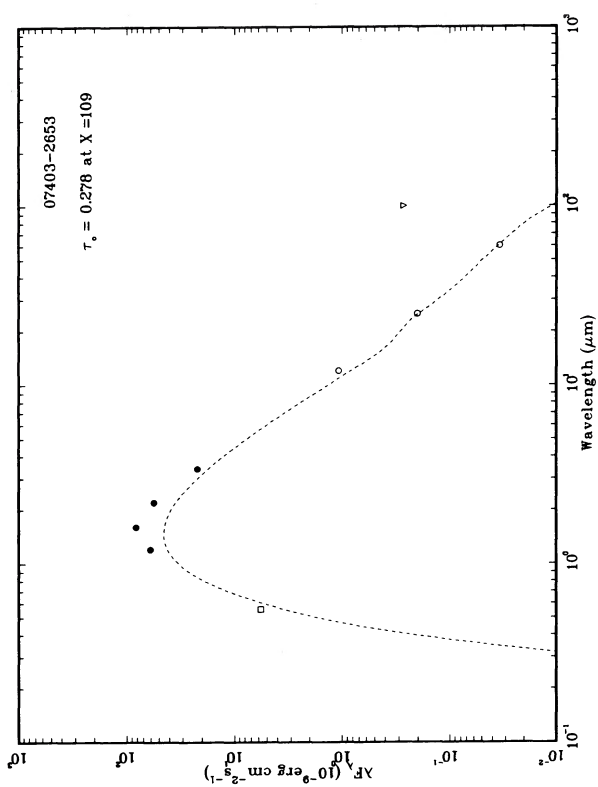


FIG. 10f

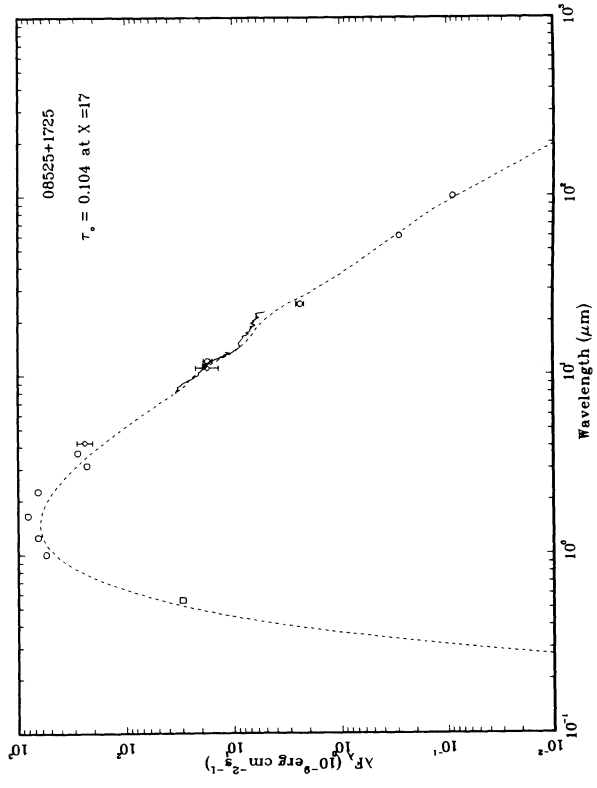
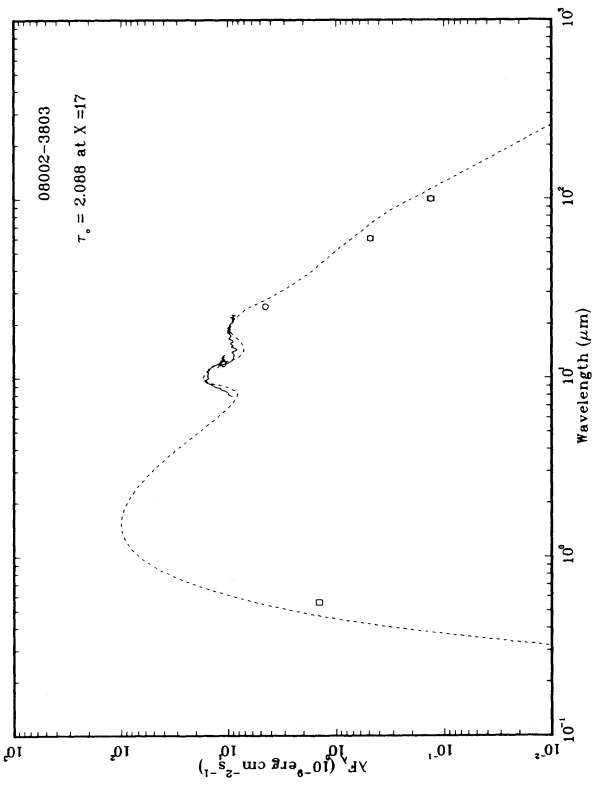
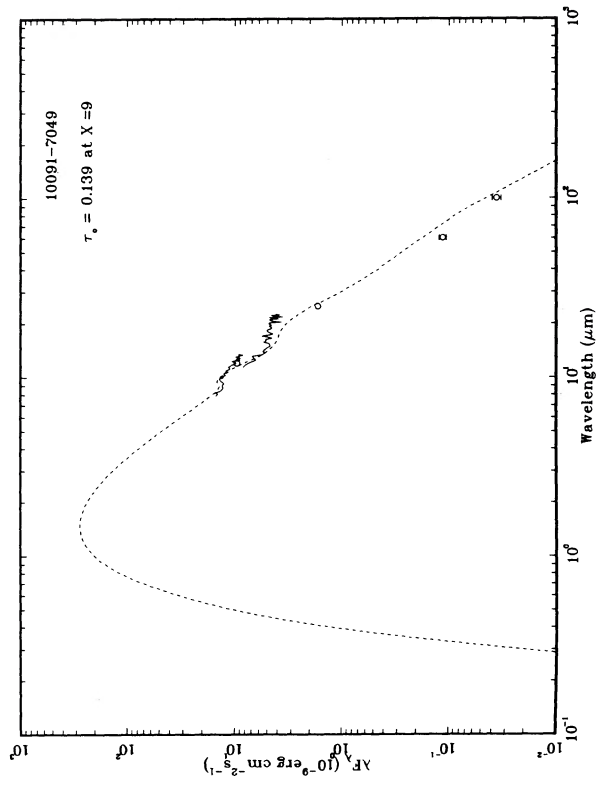
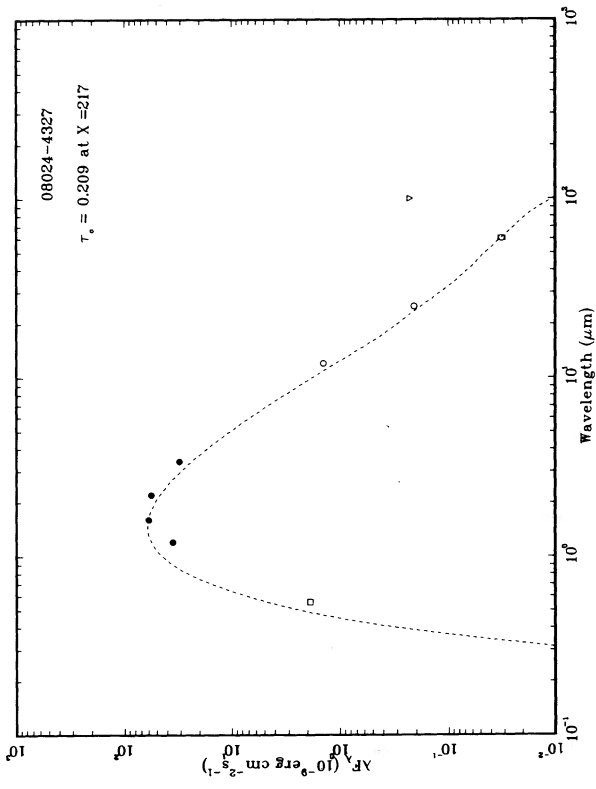


FIG. 10g

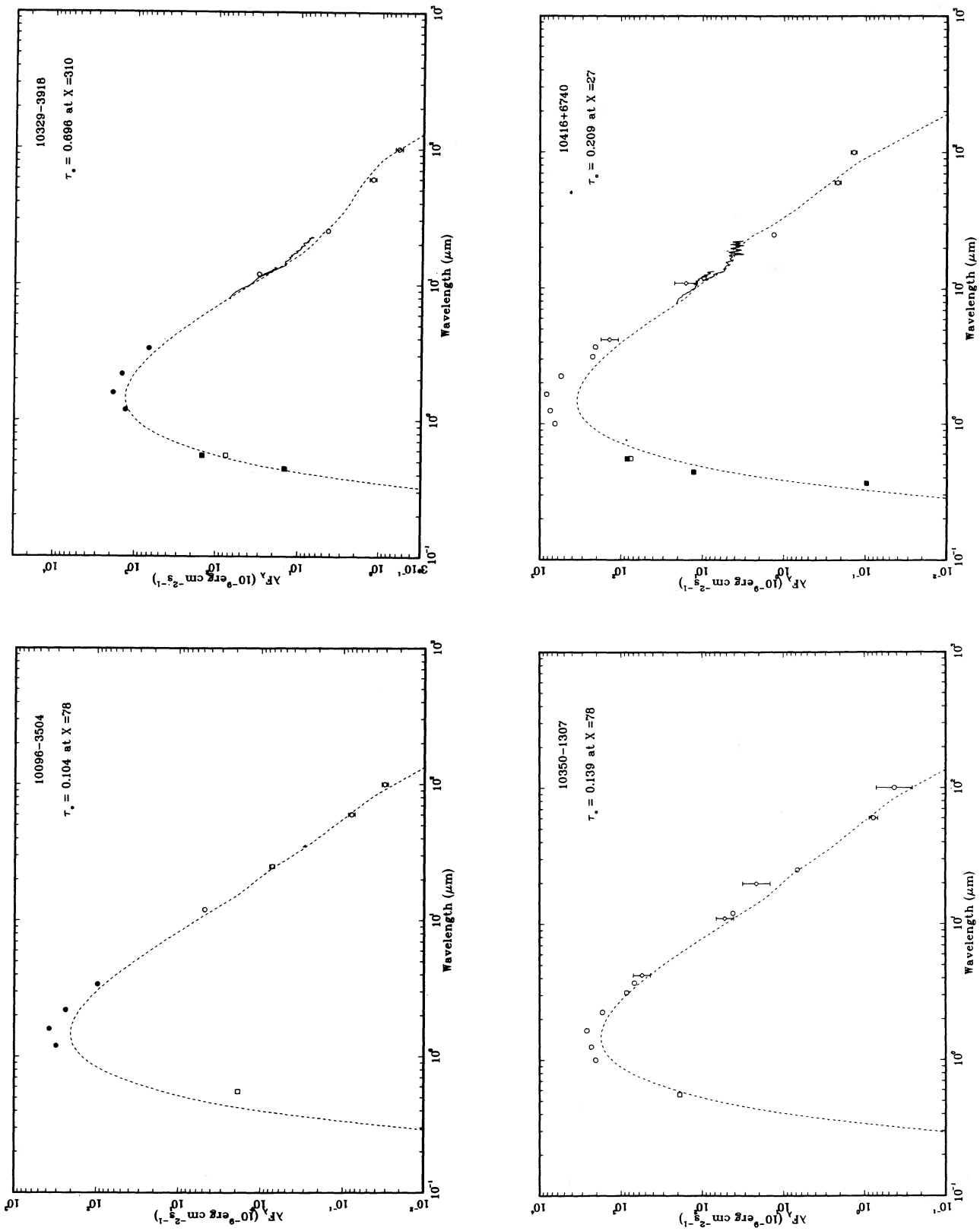


FIG. 10h

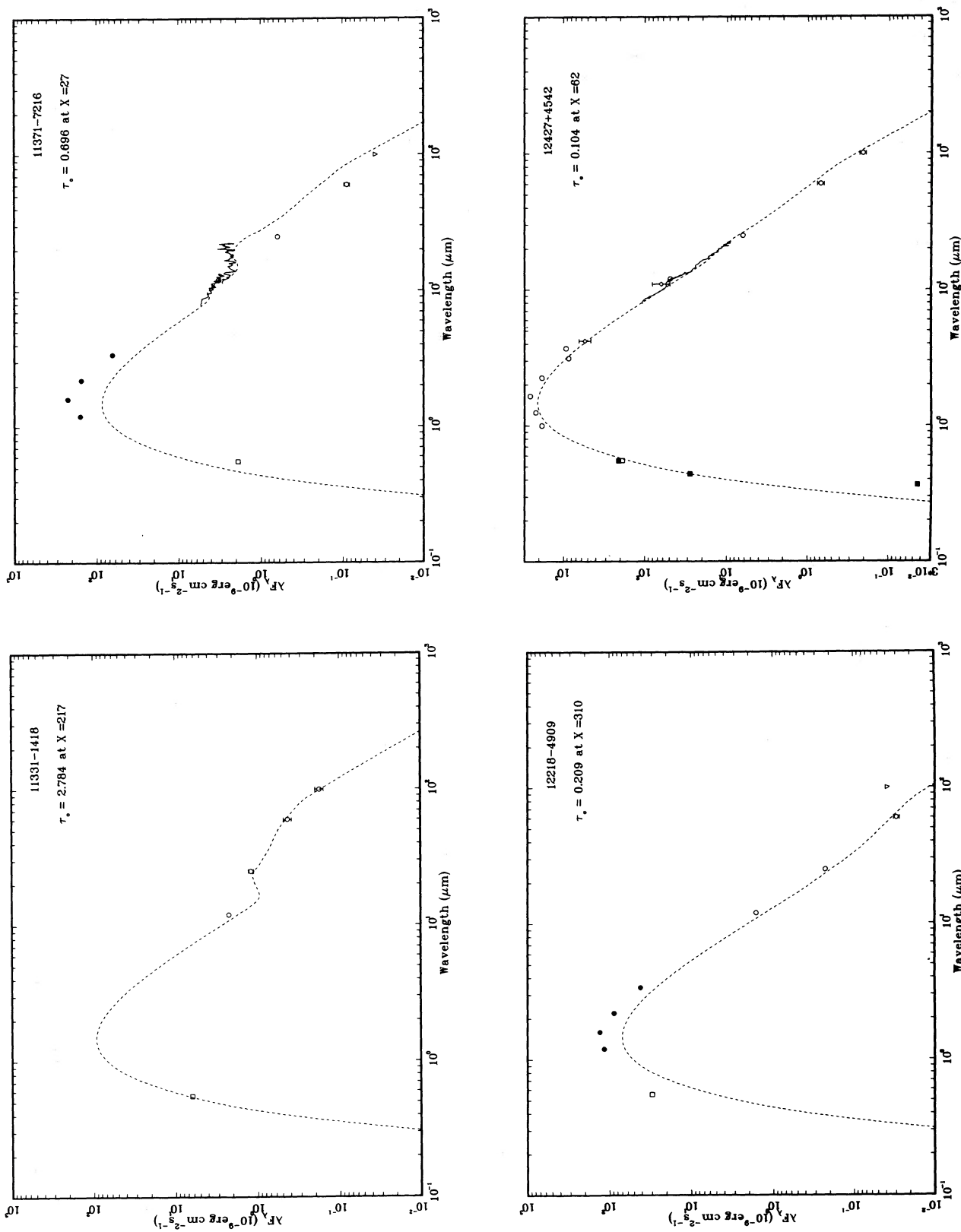


FIG. 10i

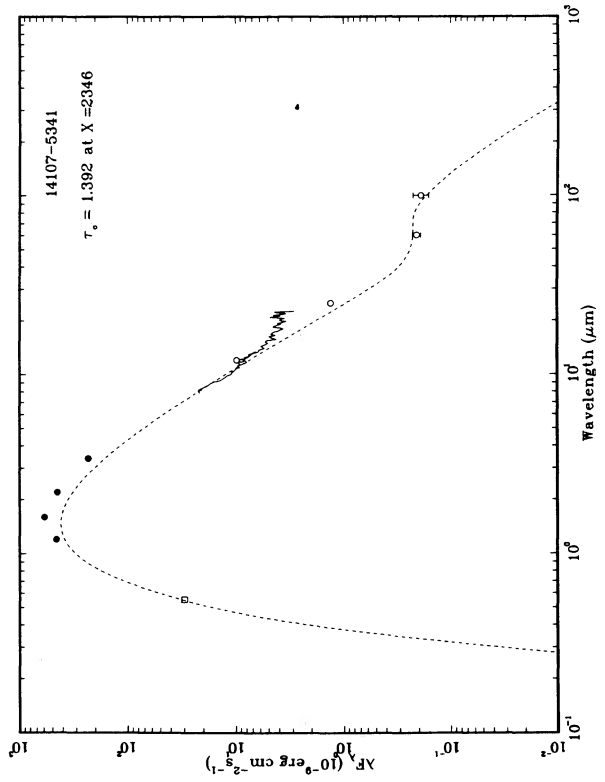
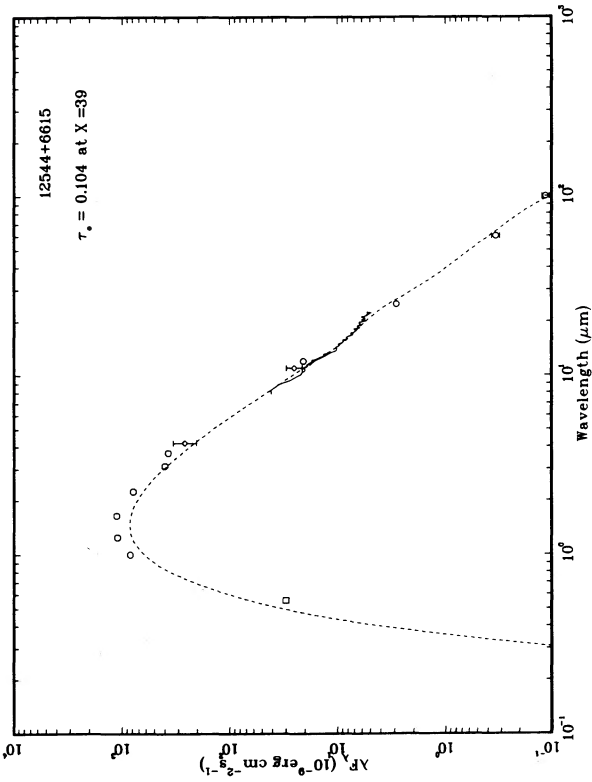
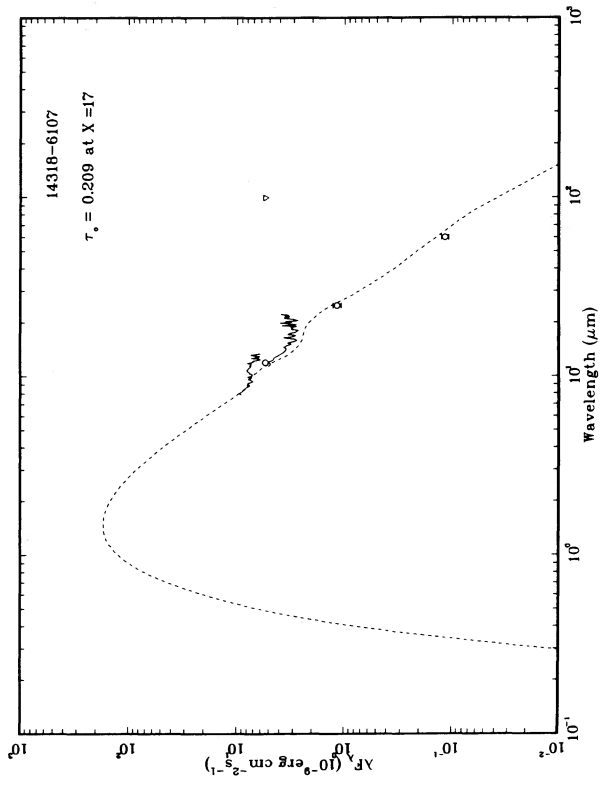
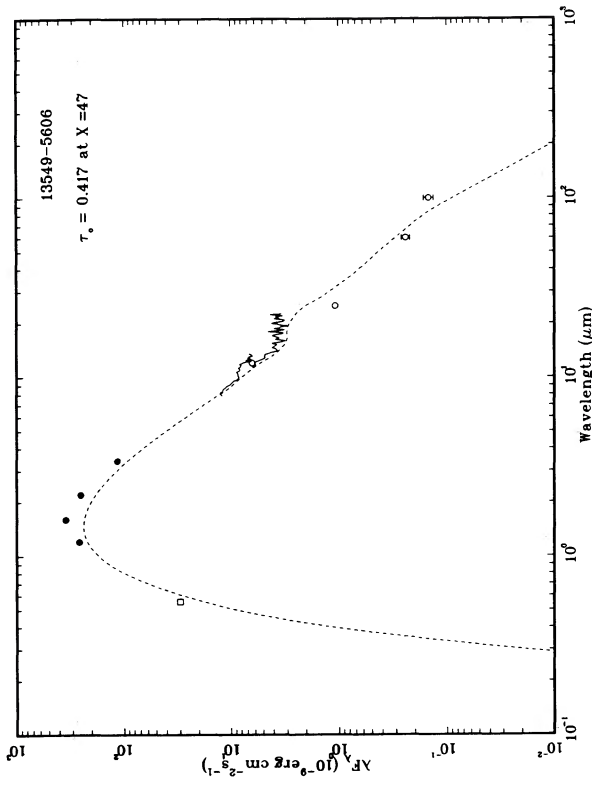


FIG. 10j

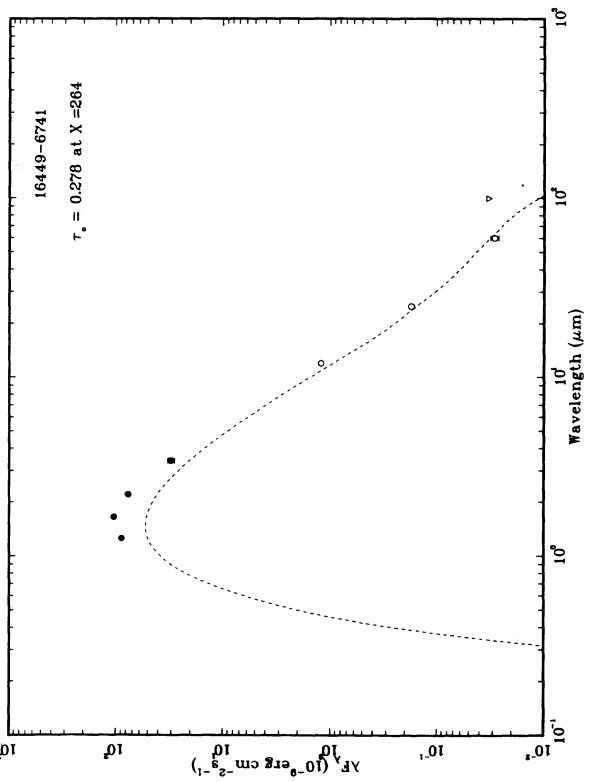
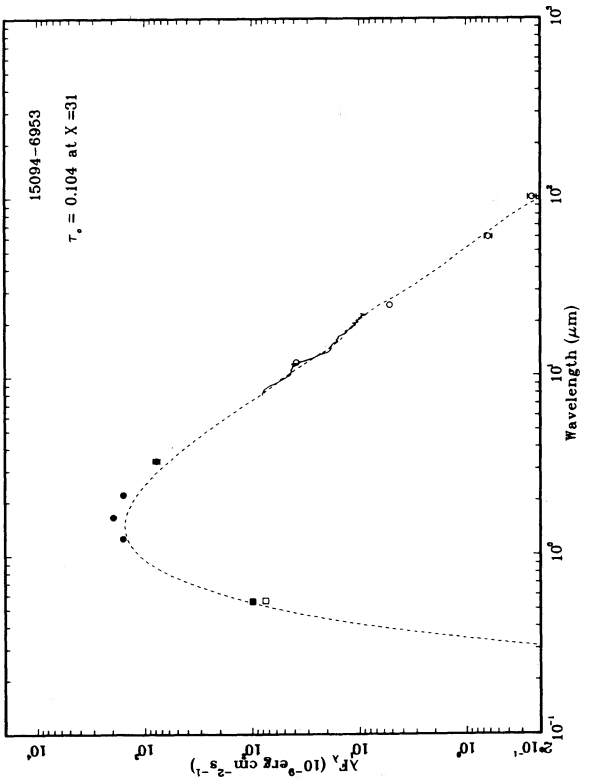
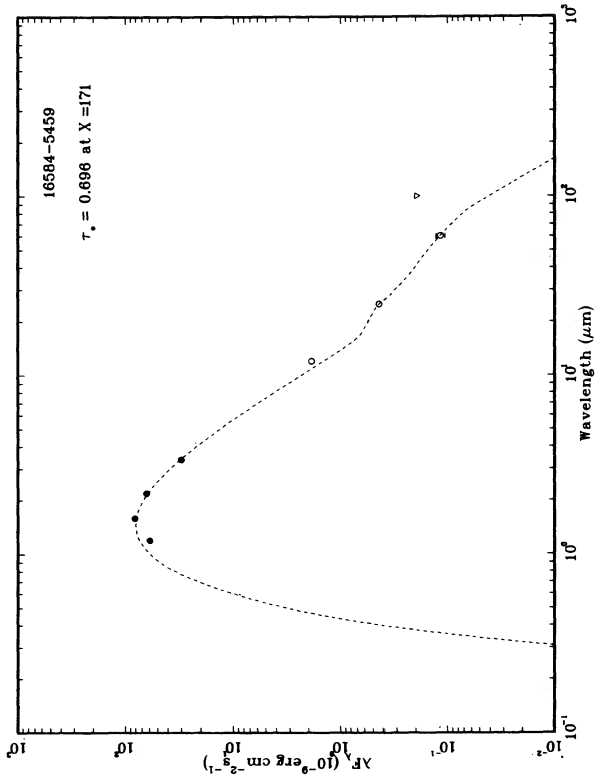
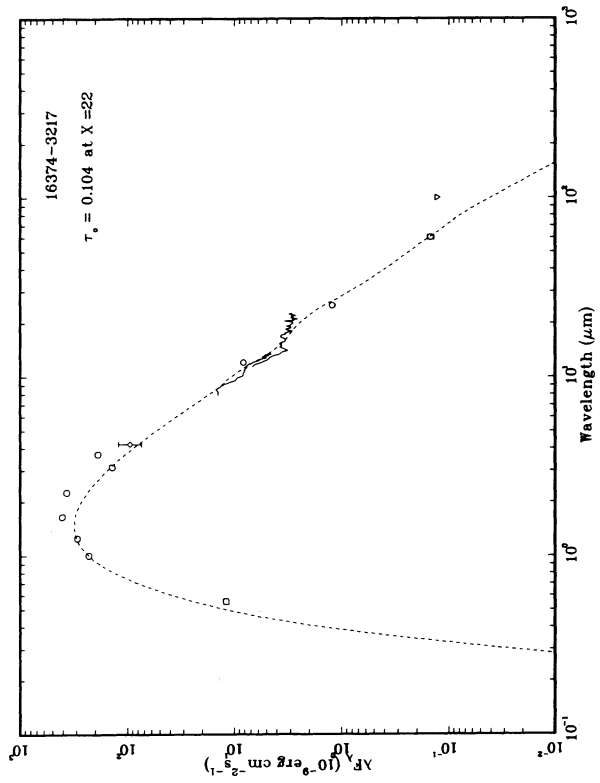


FIG. 10k

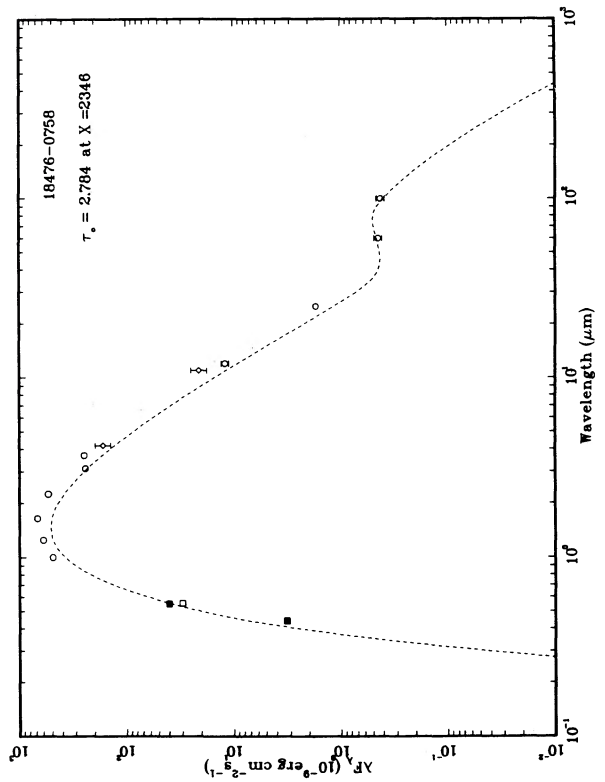
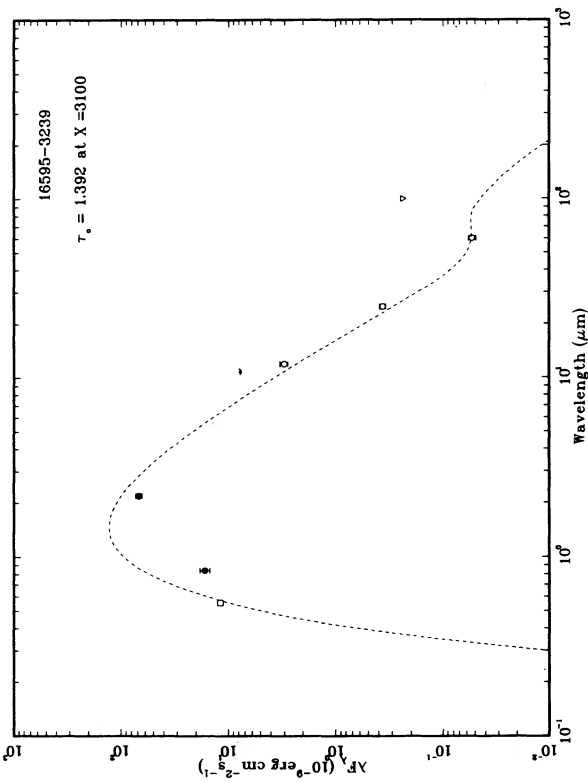
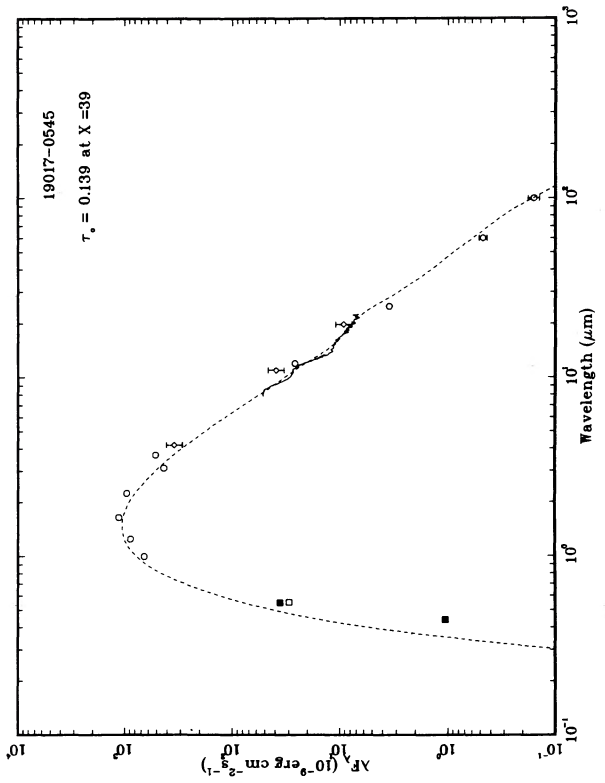
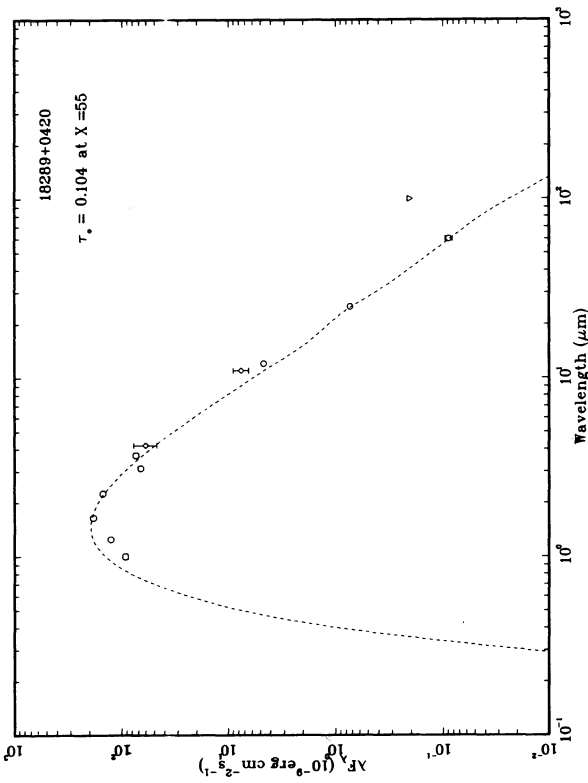


FIG. 10/

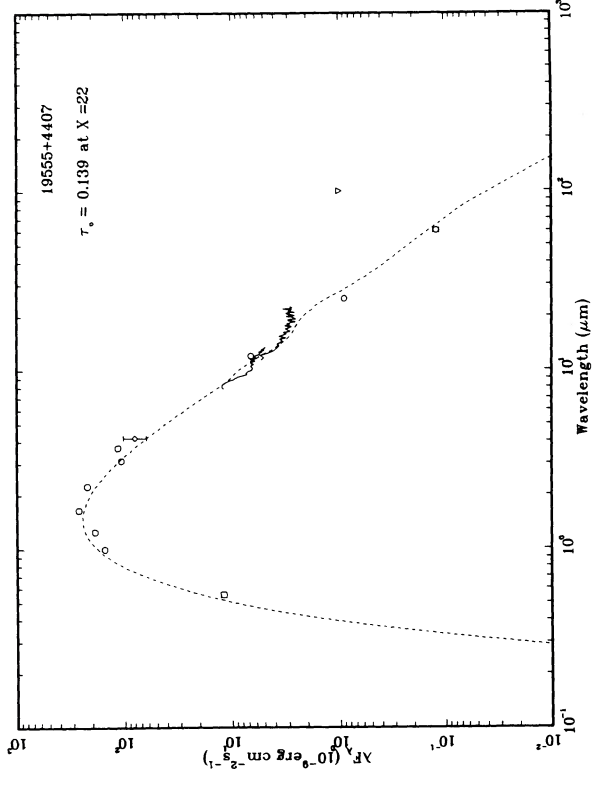
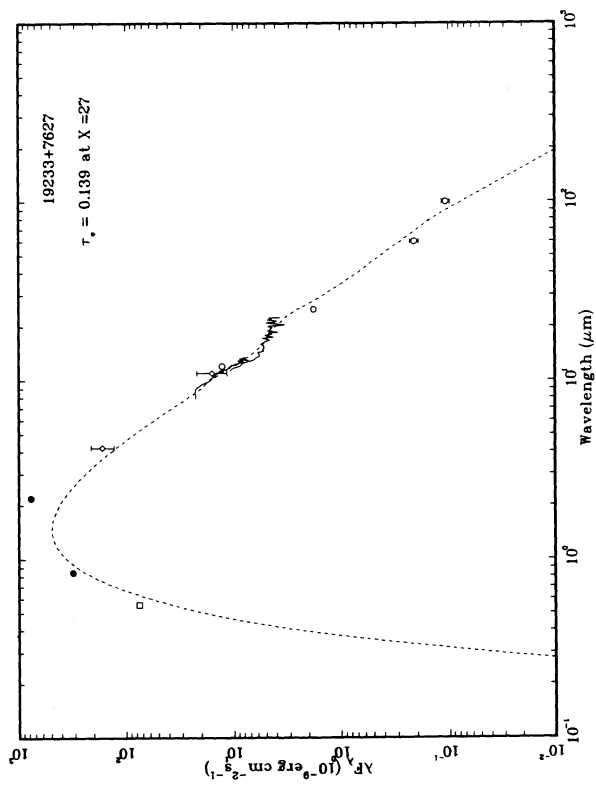
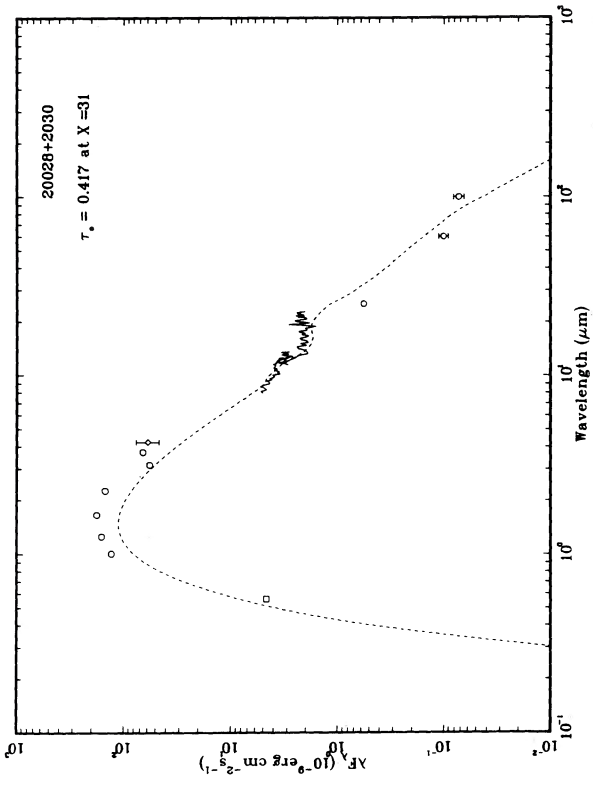
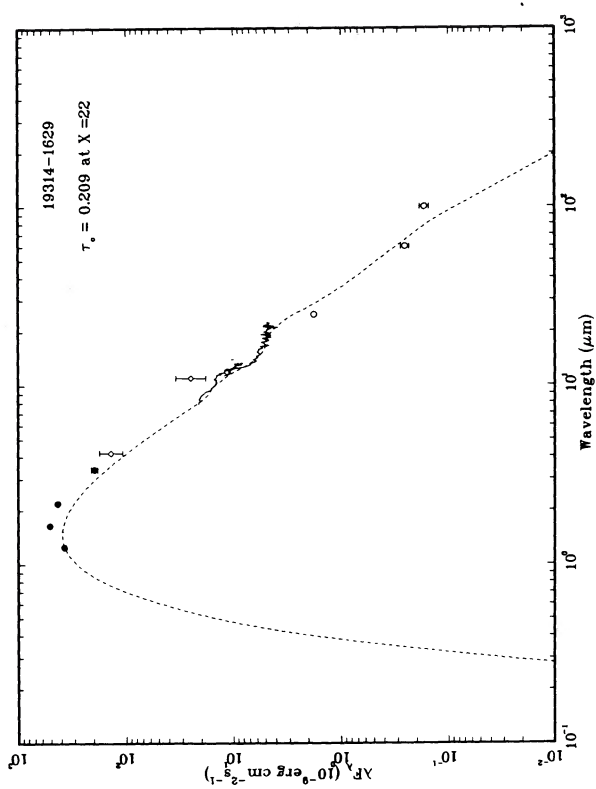


FIG. 10m

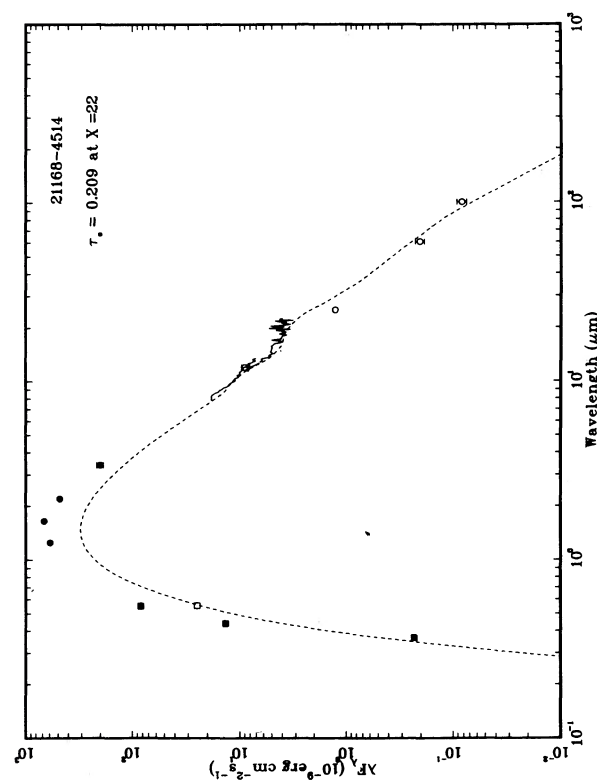
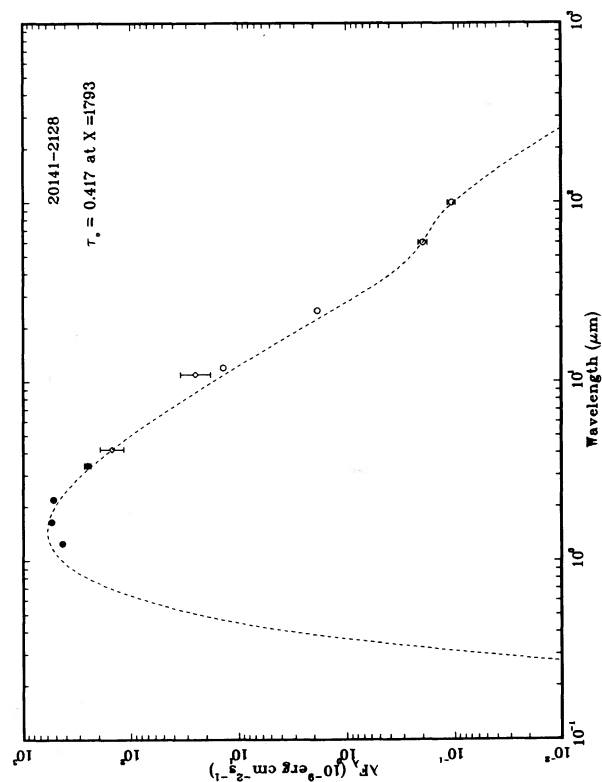
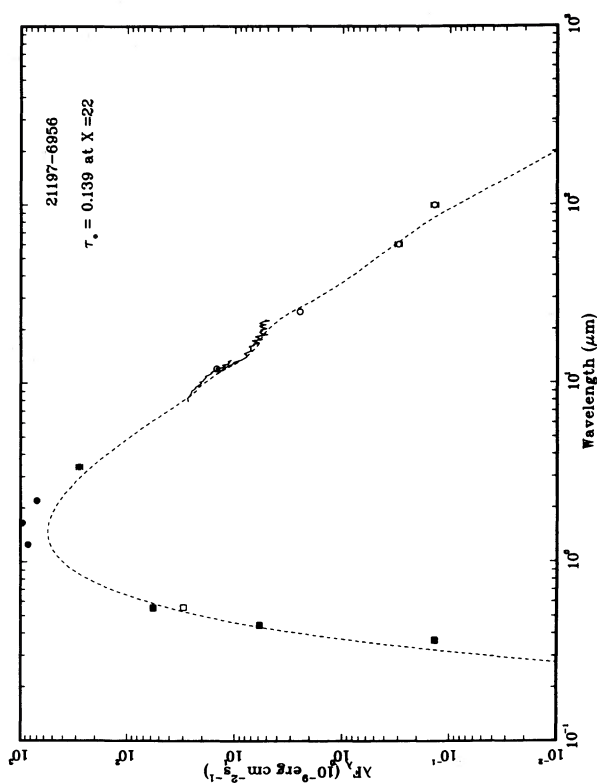
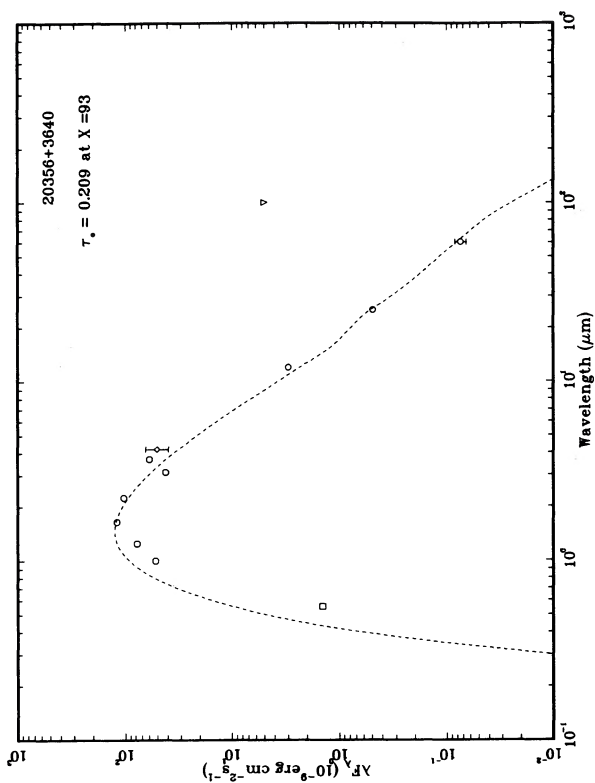


FIG. 10n

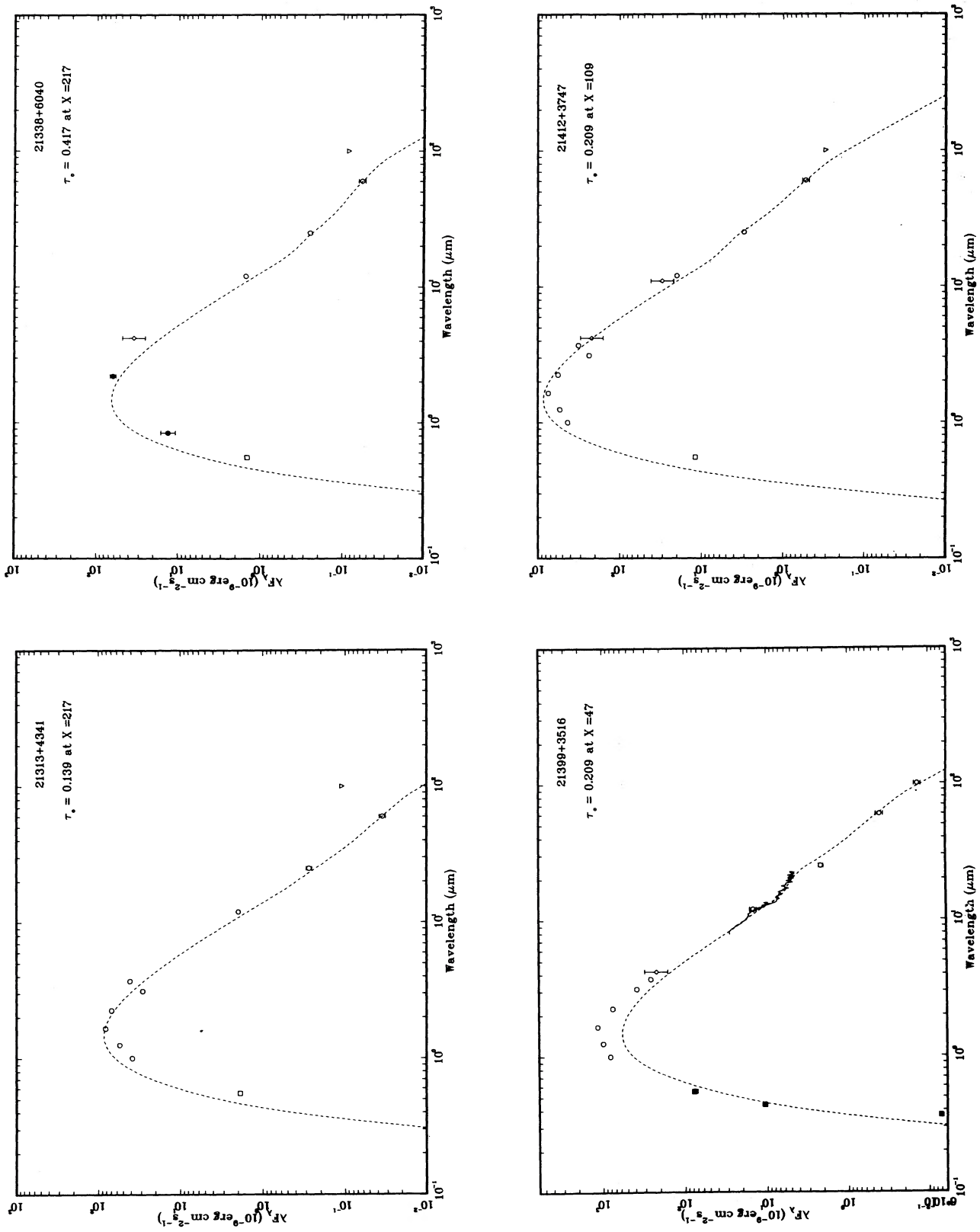


FIG. 100

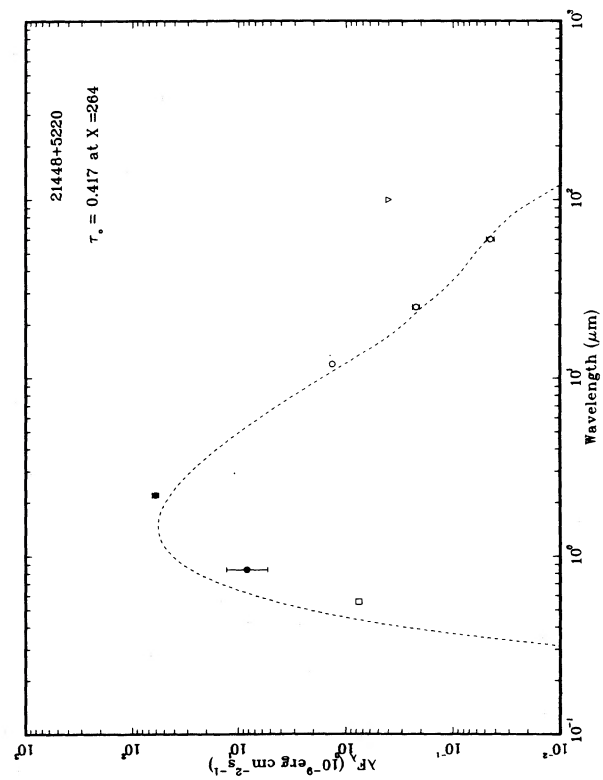
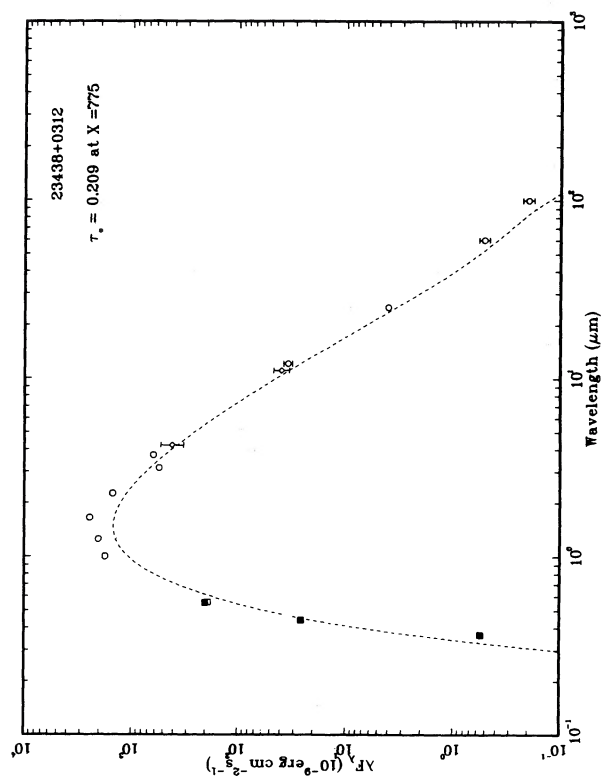


Fig. 10p

TABLE 2A
MODEL-FITTING PARAMETERS FOR STARS SHOWN IN FIGURE 10

IRAS	C	LRS	VAR (GCVS)	D (pc)	τ_o	x	IRAS	C	LRS	VAR (GCVS)	D (pc)	τ_o	x
00326+7014	21	-	Lb	1421	0.139	264	10416+6740	1736	42	Lb	662	0.209	27
00519+5817	38	-	M	1408	0.139	109	11331-1418	1886	-	-	1284	2.784	217
01133+2530	63	22	SRb	844	0.209	17	11371-7216	1901	17	SRb	1321	0.696	27
03242+4400	143	-	M	1991	0.278	124	12218-4909	1993	-	SR	1484	0.209	310
04455-3617	250	-	SR	1247	0.067	543	12427+4542	2030	42	SRb	273	0.104	62
04459+6804	240	42	SRb	483	0.104	17	12544+6615	2047	41	SRb	426	0.104	39
04505+2241	264	-	-	1459	0.209	264	13549-5606	2134	42	-	802	0.417	47
04595+5033	277	42	Lb	815	0.209	22	14107-5341	2148	18	-	608	1.392	2346
05305+0707	364	-	SRb	887	0.139	93	14318-6107	2172	16	-	940	0.209	17
05418-4628	398	41	Lb	620	0.209	27	15094-6953	2219	42	Lb	317	0.104	31
05421+2424	390	42	-	831	0.278	27	16374-3217	2353	42	SR	696	0.104	22
05425+1529	394	-	Lb	1694	6.959	4650	16449-6741	2362	-	Lb	1711	0.278	264
05450+4453	400	-	SR	1586	0.209	171	16584-5459	2384	-	SR	1382	0.696	171
06077+2601	461	-	SRb	515	0.139	171	16595-3239	2388	-	-	1093	1.392	3100
06209+2503	501	-	M	1513	0.139	124	18289+0420	2602	-	Lb	889	0.104	55
06225+1445	508	16	Lb	739	0.209	17	18476-0758	2666	-	SR	548	2.784	2346
06450+0044	584	-	Lb	1555	0.696	388	19017-0545	2695	42	SRb	379	0.139	39
06528-4218	623	42	-	802	0.278	22	19233+7627	2738	23	SRa	559	0.139	27
07129+0509	695	-	-	1319	0.104	124	19314-1629	2744	43	SRb	625	0.209	22
07179+2505	716	29	Lb	1392	0.696	6	19555+4407	2833	42	Lb	792	0.139	22
07338+0211	815	-	-	1570	0.417	310	20028+2030	2853	17	SR	1161	0.417	31
07403-2653	869	-	-	1841	0.278	109	20141-2128	2882	-	SRb	509	0.417	1793
07452-1149	897	-	-	1604	0.104	109	20356+3640	2918	-	-	1105	0.209	93
08002-0159	999	-	-	2117	2.784	620	21168-4514	3013	17	SRb	704	0.209	22
08002-3803	1003	27	-	1182	2.088	17	21197-6956	3018	22	SRb	527	0.139	22
08024-4327	1027	-	-	1589	0.209	217	21313+4341	3040	-	Lb	1342	0.139	217
08525+1725	1338	42	SRb	495	0.104	17	21338+6040	3045	-	-	1540	0.417	217
10091-7049	1633	22	-	741	0.139	9	21399+3516	3060	42	Lb	516	0.209	47
10096-3504	1630	-	-	867	0.104	78	21412+3747	3063	-	SRb	425	0.209	109
10329-3918	1706	21	SR	341	0.696	310	21448+5220	3069	-	SRb	1644	0.417	264
10350-1307	1714	-	SRb	295	0.139	78	23438+0312	3202	-	Lb	322	0.209	775

that the process of SiC grain formation may have already begun.

c) Carbon Stars with Silicate Features

One of the original motivations of the model of Willems and de Jong (1988) was the discovery of carbon stars with circumstellar silicate features. Three were identified by Little-Marenin (1986), and a list of nine was given by Willems and de Jong (1986). A plot of these objects in the color-color diagram shows that they all are in the vicinity of Mira variables and cannot be distinguished from class 20 objects strictly by their color. This implies that the appearance of the carbon-enriched photosphere is almost coincident with the termination of mass loss. Figure 10c shows a fit of the spectrum of BM Gem (07179+2505), one of the carbon stars with the $10\ \mu\text{m}$ feature. The small excess at $60\ \mu\text{m}$ suggests that the dust shell is barely detached ($t \sim 16\ \text{yr}$). The presence of strong silicate features

only in carbon stars with small detachment times is consistent with the model spectral evolution in Figure 9, which shows that the strength of the silicate feature quickly diminishes as the circumstellar envelope expands and the optical depth at $10\ \mu\text{m}$ decreases.

An alternative explanation of the presence of silicate features in carbon stars is that the silicate feature originates from an unseen M star component in a binary system (Little-Marenin 1986). If this is the case, then it would be useful to detect other properties of the M star. Three candidates (V778 Cyg = IRAS 20350+5954, BM Gem, and EU And = IRAS 23176+4658) were searched for H_2O maser emission by Benson and Little-Marenin (1987) and by Nakada *et al.* (1987). V778 Cyg was detected by Nakada *et al.* with excellent positional and velocity coincidence with the optical star (Deguchi *et al.* 1988), while EU And was detected by Benson and Little-Marenin but not by Nakada *et al.* BM Gem was not detected by either group. In

TABLE 2B
MODEL-FITTING PARAMETERS FOR CARBON STARS WITH NO LRS

IRAS	C	VAR (GCVS)	D (pc)	τ_{\odot}	x	IRAS	C	VAR (GCVS)	D (pc)	τ_{\odot}	x
00197+5854	13	Lb	1512	0.139	109	08158-3326	1116	-	1752	0.278	217
01441+5848	83	-	4155	2.784	543	08243-1704	1174	-	1609	0.209	217
03189+5550	140	-	2008	0.278	124	08265-3641	1187	-	2118	0.417	217
03364+6055	151	-	1511	0.209	217	08461-7051	1307	-	1894	0.139	264
03486+4337	161	Lb	1922	0.696	388	09054-5622	1388	-	2152	0.278	217
04360+4131	230	Lb	1832	0.139	217	09149+5136	1412	Lb	1688	0.139	217
04363+3855	231	Lb	1835	0.209	310	09191-4648	1435	-	1732	0.696	388
05026+3721	282	Lb	1862	0.209	109	09311-4105	1487	-	1642	0.139	310
05030+4006	283	-	2587	0.696	264	09339-5126	1505	-	1419	0.139	47
05217+3346	327	-	3484	4.175	620	09417-4631	1531	SRb	1642	0.209	124
05356+3025	376	-	2714	1.392	465	09535-4938	1584	L	2032	0.417	388
05427+2528	392	-	2540	4.175	543	10227-5451	1676	-	1780	0.209	93
05495+2953	415	-	2197	0.417	171	11374-5818	1902	-	1565	0.209	109
05550+2827	429	-	1459	0.104	109	11452-5734	1917	-	2351	0.696	310
05589+2731	439	-	2160	0.209	124	11548-5645	1937	-	1493	0.139	62
06152-0013	482	-	1831	0.104	62	13342-6232	2105	-	1186	2.088	217
06208-0725	504	-	1781	0.139	109	15053-5322	2214	-	2885	2.088	465
06381+1237	556	-	2133	0.209	124	17565-5555	2505	-	1677	0.067	62
06408-0842	568	-	1669	0.209	217	18153-0601	2562	-	3199	4.175	620
06427+0943	575	-	2086	0.696	264	19415+1926	2782	Lb	1503	0.139	171
06439-1249	579	-	1891	0.139	124	19481+3053	2811	-	1759	0.417	217
06489-0511	597	-	3538	2.784	543	19505+5333	2823	M	1884	0.139	55
06525-0757	614	SRa	1830	0.278	264	20001+2056	2843	Lb	2039	0.209	109
06536+0708	621	SR	2353	0.696	264	20321+4909	2911	-	2409	1.392	465
07204-1032	738	-	1699	0.209	78	21174+4531	3020	-	2265	0.696	264
07215-2252	747	Lb	1708	0.139	171	21458+4539	3071	Lb	1533	0.417	388
07220-0050	748	-	1546	0.067	109	22442+5919	3158	-	1302	0.209	62
07317-2220	807	-	2954	1.392	388	22454+5802	3159	-	3668	4.175	465
07500-4608	931	-	1666	0.209	109	22539+5357	3171	Lb	2228	0.696	465
07509-1121	932	-	1134	0.278	39	23384+7002	3198	-	2040	0.104	31
08105-3855	1090	-	1828	0.417	310						

TABLE 3
COMPARISON OF MASS-LOSS RATES DERIVED FROM INFRARED AND CO DATA

IRAS NAME	INFRARED (our model)		CO		Reference
	\dot{M} ($M_{\odot} \text{ yr}^{-1}$)	D (pc)	\dot{M} ($M_{\odot} \text{ yr}^{-1}$)	D (pc)	
01133+2530.....	3 (-7)	844	4.0(-8)	580	1
06077+2601.....	2 (-7)	515	5.3(-7)	630	1
08525+1725.....	1.5(-7)	495	2.4(-7)	460	1
10416+6740.....	3 (-7)	662	1.3(-7)	520	1
12427+4542.....	1.5(-7)	273	{ 9.0(-8)	350	2
			{ 1.1(-7)	280	1
12544+6615.....	1.5(-7)	426	1.8(-7)	450	1
19017-0545.....	2 (-7)	379	1.4(-7)	370	1
19233+7627.....	2 (-7)	559	1.8(-7)	430	1

REFERENCES.—(1) Olofsson, Eriksson, and Gustafsson 1987; (2) Knapp and Morris 1985.

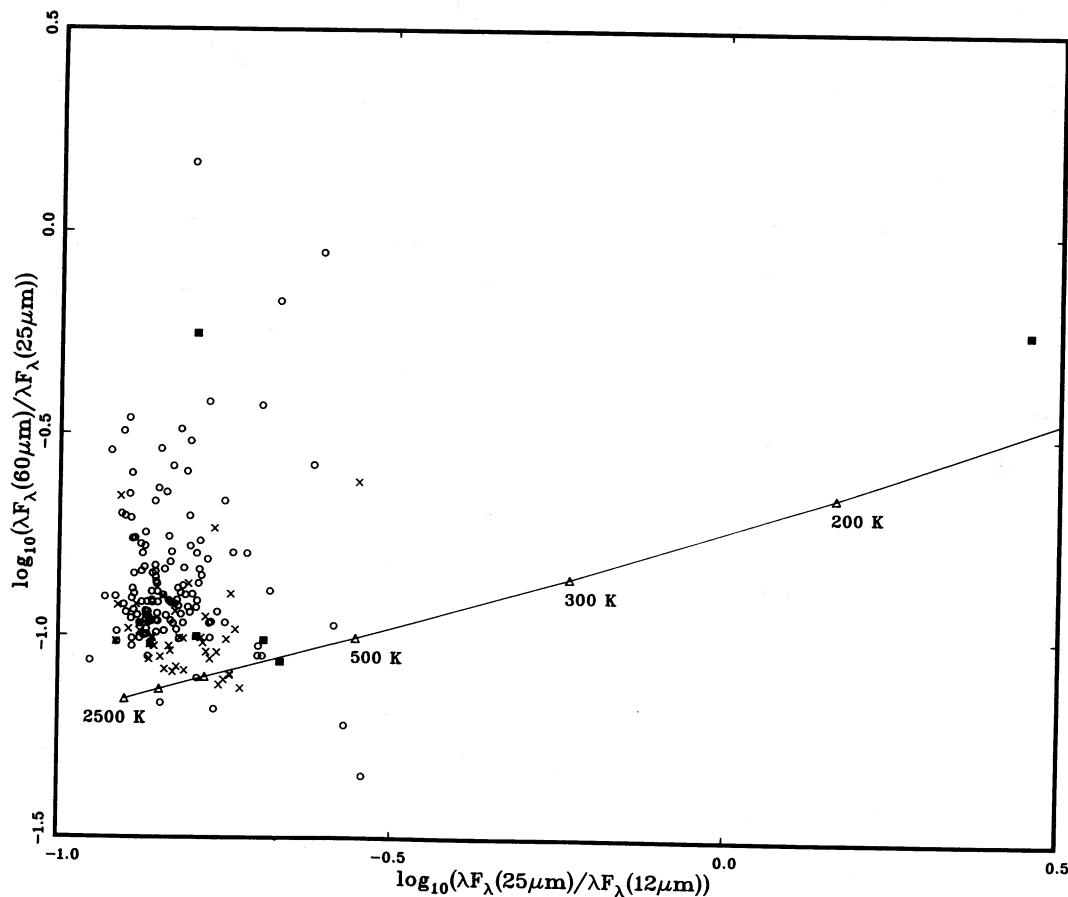


FIG. 11.—Distribution of large-amplitude (*crosses*) and small-amplitude (*open circles*) visual carbon stars in the color-color diagram. All other variable types are shown as filled squares.

view of the presence of H_2O in V778 Cyg and the fact that H_2O maser is likely to be excited in the inner parts of the circumstellar envelopes of oxygen-rich stars, it appears that V778 Cyg may indeed be a binary. The position of this object on the color-color diagram is certainly consistent with the infrared component being a Mira variable.

In the cases of EU And and V778 Cyg, Little-Marenin, Benson, and Little (1987) also note that these stars have been known carbon stars for ~ 50 yr, and this period may be too long for them to be transition objects. The silicate emission features in both objects are very strong (LRS class 29), whereas our model indicates that the silicate features should disappear after ~ 100 yr. It is therefore probable that the silicate features are not related to the carbon star. In fact, we find that a good fit cannot be obtained for the spectrum of V778 Cyg using the detached-shell model.

Our inability to reproduce strong silicate features in carbon stars suggests that at least some of the objects with silicate features may not be transition objects after all. However, as we have shown in this paper, the strength of the detached-shell model really lies in its ability to fit the far-infrared excess of visible carbon stars, and the presence of the silicate features may be irrelevant.

d) Nature of the Infrared Excess

The origin of the controversy between Thronson *et al.* (1987) and Zuckerman (1987) can be traced to the fact that there are two kinds of carbon stars: class A carbon stars which are in

transition from oxygen-rich to carbon-rich before the large-scale formation of carbon-based grains, and class B carbon stars which are losing mass at a high rate after the formation of SiC and amorphous carbon. While Thronson *et al.* (1987) draw their sample primarily from class A sources, Zuckerman (1987) concentrates on class B sources. The infrared spectra of class A sources have two components: one photospheric and the other due to the dust shell which only manifests itself in the far-infrared ($\lambda > 20 \mu\text{m}$). The infrared spectra of class B sources, however, are dominated by dust continuum emission, and the underlying photospheres are not always visible. CO emission is predominantly associated with class B carbon stars. Comparison of the spectra of class A sources in Figure 10 with the infrared spectra of CO-emitting class 40 sources in Leahy, Kwok, and Arquilla (1987) clearly illustrates the difference. The class B sources have color temperatures ~ 500 K, which are certainly not photospheric in origin.

e) Evolution from Class A to Class B

At the end of the evolutionary track of Figure 8, carbon stars will have a very small [60/25] excess. In fact, a comparison of Figures 1a and 2a suggests that some visual carbon stars have already developed SiC features at the end of the track. It is reasonable to assume that these stars will then evolve along the C-shaped curve on Figure 2a, and later become radio carbon stars.

Our class A objects are basically equivalent to the carbon star sample of Thronson *et al.* (1987). These authors estimate

that $\sim 25\%$ of all carbon stars lie outside the color domain of their sample. Zuckerman (1987), on the other hand, maintains that the figure should be 75%. If the scenario outlined in Willems and de Jong (1988) is correct, there should be roughly equal numbers in classes A and B because they represent consecutive evolutionary stages. Any difference in number between the two groups only reflects the relative lifetimes of the two stages. Assuming that the objective-prism surveys and the infrared surveys have approximately equal efficiencies in the discovery of carbon stars, and that the numbers of objects in classes A and B are roughly comparable, then the transition time of a few times 10^4 yr discussed in § VII implies a comparable lifetime for the subsequent high-mass-loss phase. This estimate is in agreement with the observed dynamical age of $\sim 15,000$ yr for the circumstellar envelope of IRC +10216 derived from the CO brightness distribution (Knapp *et al.* 1982).

The model calculations of this paper have not considered the formation of carbon-based grains and the renewed mass loss after the formation of carbon grains because our treatment is limited to the optically thin case. It is clear from the spectra of class B objects that they are optically thick in the infrared, and a proper radiative transfer calculation has to be performed. This will be the subject of our second paper (Chan and Kwok 1989).

f) S Stars

S stars are often suggested as transition objects between M and C stars (see, e.g., Jura 1988). A cross-reference check of the *General Catalogue of S Stars* (Stephenson 1976) and the *IRAS Point Source Catalog* shows that S stars belong to both LRS class 20 (oxygen-rich) and LRS class 40 (carbon-rich). A plot of their color distribution also shows overlap with both visible carbon stars and oxygen-rich stars. We find no obvious unique infrared property which characterizes S stars as a separate group.

g) Ratio of Carbon Stars to Oxygen-rich Stars

If visual carbon stars are indeed transition objects, as suggested by Willems and de Jong (1988), then our calculations show that the lifetime of visual carbon stars (class A) objects is $\sim 5 \times 10^4$ yr. Assuming that most oxygen-rich stars which attain a certain luminosity become carbon stars, then the observed number ratio of oxygen-rich to carbon stars of ~ 10 to 1 implies a lifetime of $\sim \frac{1}{2}$ Myr for oxygen-rich stars. The total lifetime of stars on the AGB depends on both the nuclear burning rate and the mass-loss formula. In the model of Volk and Kwok (1988a), the lifetime on the AGB (after the early AGB stage, Iben and Renzini 1983) ranges from 1.1×10^6 to 0.5×10^6 yr for stars of initial mass of 1.5 – $8 M_{\odot}$. These values are within a factor of 2 of the prediction and are probably acceptable in view of the uncertainty in the estimate of the relative sizes of the oxygen-rich and carbon star samples.

We may further speculate that evolution on the AGB leads to two separate branches. Some of the Mira variables (class 20 objects) will undergo a surface composition change and evolve to carbon stars as in Figure 8. However, others may stay oxygen-rich and develop higher mass-loss rates and become silicate absorption objects (class 30) and evolve according to Figure 12 of Volk and Kwok (1988a). It would be interesting in the next few years to determine further the fraction of AGB stars which take each of these two pathways and further explore the physics behind the branching into carbon stars.

IX. CONCLUSIONS

Optical, infrared, and radio observations have led to three different ways of identifying a carbon star, and the objects identified by these different methods are not entirely overlapping. The *IRAS* sky survey shows that these three sets have intrinsically different infrared colors. Visual carbon stars have large $60 \mu\text{m}$ excesses, whereas radio carbon stars have blackbody-like energy distributions. Infrared carbon stars are a mixture in behavior of the above two groups. A recent theory of Willems and de Jong (1988) suggests that the visual carbon stars represent an intermediate evolutionary stage between the Mira variables and radio/infrared carbon stars. We have performed calculations to obtain the spectra and simulated *IRAS* colors of objects in transition from oxygen-rich to carbon-rich. The results are in excellent agreement with observations. By fitting the observed spectra of individual stars with the models, we are able to obtain the mass-loss rate of the star when it was a Mira and the time elapsed since the termination of that mass loss, as well as the distance. Since these parameters are derived from assumed values of the luminosity, photospheric temperature, and outflow velocity, they are only intended for the illustration of the statistical properties of carbon stars but are not intended for individual objects which may have properties which depart from the assumed values. The transition time from the Mira stage to a radio/infrared carbon star is estimated to be $\sim 5 \times 10^4$ yr.

Although the presence of silicate features in certain carbon stars provides the original motivation of the theory of Willems and de Jong, we find that the silicate features in these objects are too strong to be transition objects. This discrepancy, however, should have no bearing on the correctness of the detached-shell model, for the spectra of a large number of other carbon stars can be successfully fitted by the model.

We also support the conclusion of Willems and de Jong that the near-infrared ($\lambda < 10 \mu\text{m}$) continuum of visual carbon stars is dominated by photospheric emission. The dust envelopes of visual carbon stars manifest themselves only beyond about $20 \mu\text{m}$. The difference in the nature of the infrared emission between visual and radio/infrared carbon stars suggest that they represent distinct stages of AGB evolution and cannot be treated as one uniform sample.

The previous confusing picture of the origin of carbon stars is now greatly clarified. Carbon stars identified in the visible region are most likely objects in transition between two mass-losing episodes. We hope that this paper will stimulate further observations of transition objects and lead to a better understanding of branching into carbon stars on the AGB.

We thank Dr. F. Willems for stimulating discussions during the Calgary and Leuven workshops. We also thank Dr. H. Walker for helpful information on the class 40 objects. Drs. B. Zuckerman and M. Jura provided critical comments on an earlier version of this paper. We are particularly grateful to the referee, Dr. Robert Wing, who has made numerous suggestions which have much improved the paper. This work was done in partial fulfillment of the requirements of a M.Sc. degree by S. J. C. at the University of Calgary, and was supported by the Natural Sciences and Engineering Research Council of Canada.

REFERENCES

- Arquilla, R., Leahy, D. A., and Kwok, S. 1986, *M.N.R.A.S.*, **220**, 125.
- Bell, M. B., Feldman, P. A., Kwok, S., and Matthews, H. E. 1982, *Nature*, **295**, 389.
- Benson, P. J., and Little-Marenin, I. R. 1987, *Ap. J. (Letters)*, **316**, L37.
- Blanco, B. M., Blanco, V. M., and McCarthy, M. F. 1978, *Nature*, **271**, 638.
- Blanco, V. M., McCarthy, M. F., and Blanco, B. M. 1980, *Ap. J.*, **242**, 938.
- Chan, S. J., and Kwok, S. 1988, in preparation.
- Cohen, J. G., Frogel, J. A., Persson, S. E., and Elias, J. H. 1981, *Ap. J.*, **249**, 481.
- Deguchi, S., Kawabe, R., Ukita, N., Nakada, Y., Onaka, T., Izumiura, H., and Okamura, S. 1988, *Ap. J.*, **325**, 795.
- Draine, B. T. 1985, *Ap. J. Suppl.*, **57**, 587.
- Forrest, W. J., Gillett, F. C., and Stein, W. A. 1975, *Ap. J.*, **195**, 423.
- Frogel, J., and Blanco, V. M. 1984, in *Observational Tests of Stellar Evolution Theory*, ed. A. Maeder and A. Renzini (Dordrecht: Reidel), p. 175.
- Fuenmayor, F. J. 1981, *Rev. Mexicana Astr. Ap.*, **6**, 83.
- Gezari, D. Y., Schmitz, M., and Mead, J. M. 1984, *Catalog of Infrared Observations*, NASA Ref. Pub. 1118.
- Gilman, R. C. 1974, *Ap. J. Suppl.*, **28**, 397.
- Habing, H. J., Olonof, F. M., Chester, T., Gillett, F., Rowan-Robinson, M., and Neugebauer, G. 1985, *Astr. Ap.*, **152**, L1.
- Hacking, P., et al. 1985, *Pub. A.S.P.*, **97**, 616.
- Hardorp, J., Lübeck, K., and Stephenson, C. B. 1973, *Astr. Ap.*, **22**, 129.
- Hoffleit, D., and Jaschek, C. 1982, *The Bright Star Catalogue* (4th rev. ed.; New Haven: Yale University Observatory).
- Iben, I., Jr. 1975, *Ap. J.*, **196**, 525.
- . 1985, in *Nucleosynthesis: Challenges and New Developments*, ed. W. D. Arnett and J. W. Truran (Chicago: University of Chicago Press), p. 272.
- . 1987, in *Late Stages of Stellar Evolution*, ed. S. Kwok and S. R. Pottasch (Dordrecht: Reidel), p. 175.
- Iben, I., Jr., and Renzini, A. 1982a, *Ap. J. (Letters)*, **259**, L79.
- . 1982b, *Ap. J. (Letters)*, **263**, L23.
- . 1983, *Ann. Rev. Astr. Ap.*, **21**, 271.
- . 1984, *Phys. Repts.*, Vol. **105**, No. 6.
- IRAS Catalogs and Atlases, Explanatory Supplement*. 1985, ed. C. A. Beichman, G. Neugebauer, H. J. Habing, P. E. Clegg, and T. J. Chester (Washington, DC: GPO).
- IRAS Science Team*. 1986, *Astr. Ap. Suppl.*, **65**, 607.
- Jura, M. 1988, *Ap. J. Suppl.*, **66**, 33.
- Knapp, G. R. 1986, *Ap. J.*, **311**, 731.
- . 1987, in *Late Stages of Stellar Evolution*, ed. S. Kwok and S. R. Pottasch, p. 103.
- Knapp, G. R., and Morris, M. 1985, *Ap. J.*, **292**, 640.
- Knapp, G. R., Phillips, T. G., Leighton, R. B., Lo, K. Y., Wannier, P. G., and Wootten, H. A. 1982, *Ap. J.*, **252**, 616.
- Kukarkin, B. V., et al. 1969, *General Catalogue of Variable Stars* (3d ed.; Moscow: Academy of Sciences of the USSR) (GCVS).
- . 1982, *New Catalogue of Suspected Variable Stars* (Moscow: Nauka).
- Kurtanidze, O. M., and West, R. M. 1980, *Astr. Ap. Suppl.*, **39**, 35.
- Kwok, S. 1975, *Ap. J.*, **198**, 583.
- Kwok, S., Hrivnak, B. J., and Milone, E. F. 1986, *Ap. J.*, **303**, 451.
- Lattanzio, J. C. 1986, *Ap. J.*, **311**, 708.
- Leahy, D. A., Kwok, S., and Arquilla, R. A. 1987, *Ap. J.*, **320**, 825.
- Likkel, L., Omont, A., Morris, M., and Forveille, T. 1987, *Astr. Ap.*, **173**, L11.
- Little-Marenin, I. R. 1986, *Ap. J. (Letters)*, **307**, L15.
- Little-Marenin, I. R., Benson, P. J., and Little, S. J. 1987, in *Fifth Cambridge Workshop on Cool Stars, Stellar Systems, and the Sun*, ed. J. L. Linsky and R. E. Stencel (New York: Springer-Verlag), p. 396.
- Lockwood, G. W. 1970, *Ap. J.*, **160**, L47.
- MacConnell, D. J. 1979, *Astr. Ap. Suppl.*, **38**, 335.
- . 1982, *Astr. Ap. Suppl.*, **48**, 355.
- Merrill, K. M., and Stein, W. A. 1976, *Pub. A.S.P.*, **88**, 874.
- Miller, J. S. 1970, *Ap. J. (Letters)*, **161**, L95.
- Nakada, Y., Izumiura, H., Onaka, T., and Hashimoto, O. 1987, *Ap. J. (Letters)*, **323**, L77.
- Neugebauer, G., and Leighton, R. B. 1969, *Two Micron Sky Survey*, NASA SP-3047.
- Nguyen-Q-Rieu, Epchtein, N., Truong-Bach, and Cohen, M. 1987, *Astr. Ap.*, **180**, 117.
- Noguchi, K., Kawara, K., Kobayashi, Y., Okuda, H., Sato, S. and Oishi, M. 1981, *Pub. Astr. Soc. Japan*, **33**, 373.
- Olofsson, H. 1987, in *The Late Stages of Stellar Evolution*, ed. S. Kwok and S. R. Pottasch (Dordrecht: Reidel), p. 149.
- Olofsson, H., Eriksson, K., and Gustafsson, B. 1987, *Astr. Ap.*, **183**, L13.
- Price, S. D., and Walker, R. D. 1976, *The AFGL Four Color Infrared Sky Survey*, Air Force Geophys. Lab. Tech. Rep. No. AFGL TR-76-0208.
- Renzini, A., and Voli, M. 1981, *Astr. Ap.*, **94**, 175.
- Stephenson, C. B. 1965, *Ap. J.*, **142**, 712.
- . 1973, *A General Catalogue of Cool Carbon Stars* (Pub. Warner & Swasey Obs., Vol. 1, No. 4) (GCCCS).
- . 1976, *A General Catalogue of S Stars* (Pub. Warner & Swasey Obs., Vol. 2, No. 2).
- . 1985, *A.J.*, **90**, 784.
- Thronson, H. A., Latter, W. B., Black, J. H., Bally, J., and Hacking, P. 1987, *Ap. J.*, **322**, 770.
- Treffers, R., and Cohen, M. 1974, *Ap. J.*, **188**, 545.
- van der Veen, W. E. C. J., and Habing, H. J. 1988, *Astr. Ap.*, **194**, 125.
- Volk, K., and Kwok, S. 1988a, *Ap. J.*, **331**, 435.
- . 1988b, in preparation.
- Wannier, P. G., and Sahai, R. 1986, *Ap. J.*, **311**, 335.
- Westerlund, B. E. 1971, *Astr. Ap.*, **4**, 51.
- Willems, F. J. 1987, Ph.D. thesis, Universiteit van Amsterdam, The Netherlands.
- Willems, F. J., and de Jong, T. 1986, *Ap. J. (Letters)*, **309**, L39.
- . 1988, *Astr. Ap.*, **196**, 173.
- Yamashita, Y. 1972, *Ann. Tokyo Astr. Obs.*, **13**, 169.
- . 1975, *Ann. Tokyo Astr. Obs.*, **15**, 1.
- Zuckerman, B. 1980, *Ann. Rev. Astr. Ap.*, **18**, 263.
- . 1987, in *Fifth Cambridge Workshop on Cool Stars, Stellar Systems, and the Sun*, ed. J. L. Linsky and R. E. Stencel (New York: Springer-Verlag), p. 351.
- Zuckerman, B., and Dyck, H. M. 1986a, *Ap. J.*, **304**, 394.
- . 1986b, *Ap. J.*, **311**, 345.
- Zuckerman, B., Dyck, H. M., and Claussen, M. J. 1986, *Ap. J.*, **304**, 401.

S. J. CHAN and S. KWOK: Department of Physics, University of Calgary, Calgary, Alberta T2N 1N4, Canada